Nanotechnology and Nanomaterials

Variation Modeling in IC Technology

H. Chen, D. S. Boning
Sponsorship: Exxon Mobil First-Year Energy Fellowship

Integrated circuit (IC) fabrication at the nanoscale is never deterministic. As the scale of microelectronic devices decreases dramatically, even small variations in the IC manufacturing process lead to significant uncertainty in the behavior of electronic devices as well as in the IC as a whole. In order to predict the variations in fabrication, various silicon IC optimization and analysis approaches have been proposed, and they are playing important roles in the IC industry. To accurately model the IC, these methods rely on testing data from the devices and circuits. However, IC testing is not free. Hundreds of test structures, such as ring oscillators, must be carefully designed, fabricated, and measured; the cost is considerable.

We are developing new techniques to model and predict variations, especially spatial variations, in IC manufacturing based on a small number of measurements. Wafer-level and die-level spatial variation data can be considered as a two-dimensional function $f(x, y)$ in which x and y are spatial coordinates of the measurement points. A Bayesian approach with frequency domain analysis is proposed to give a maximum a posteriori (MAP) estimation of the coefficients of the two-dimensional discrete cosine transform under noise. An algorithm is designed to reduce the number of frequency components to speed up the computation in large-scale problems. We also propose another fast variation estimation method based on low-rank matrix completion that transforms the estimation into an optimization problem with respect to the matrix of the variation data. We use a nuclear norm relaxation and singular value thresholding algorithm to solve this optimization problem. Penalty terms are carefully designed to take into account the different types of devices on the same die. An example is shown in Figures 1 and 2, where contact resistance data across a test chip is recovered using less than half of the measurement points. Further research will apply these methods to industrial data. Time series manufacturing data will also be studied to give an insight into the trend of variation over a large timespan.

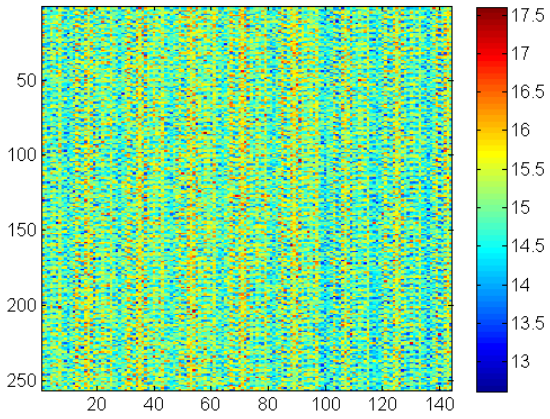

▲Figure 1: Contact resistance data (Ohms) with 256×144 measurement points.

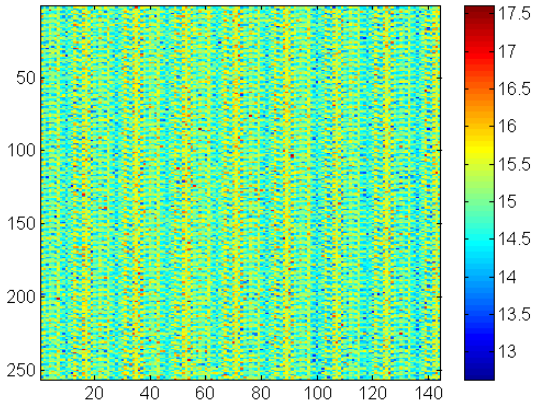

▲Figure 2: Recovered matrix with 40% measurement points randomly sampled.

FURTHER READING

- K. Balakrishnan and D. S. Boning, "Measurement and Analysis of Contact Plug Resistance Variability," *Custom Integrated Circuits Conference 2009. CICC '09*, pp. 415-422, 2009.

Characterization and Modeling of Pattern Dependencies in Spin-Coating for Advanced Packaging Technology

C. Lang, D. S. Boning
Sponsorship: Taiwan Semiconductor Manufacturing Company

Re-distribution layers (RDLs) are packaging layers dedicated to connecting separate integrated circuit (IC) chips or die to each other and to external I/O ports in advanced packaging technologies. These layers can be made smaller than the bulky metal traces in conventional substrate packaging, reducing electrical delay and power consumption. Electrochemical plating and dielectric spin-coating (DSC) can be used in wafer-scale processes to fabricate these chip-to-chip interconnects for advanced 2.5D packaging. However, non-uniformities in the underlying topography lead to surface variations in the resulting dielectric. As multiple layers are fabricated, these variations compound and can result in a structure with significant electrical parasitics.

In this study, we model and predict the non-uniformities in the DSC process caused by the underlying topographies. If these non-uniformities can be predicted, design rules can be defined that limit the resulting surface variation and enable multi-level RDL fabrication. We design test vehicles (TVs) that represent topographies common in RDLs, most notably the step heights and layout patterns of the RDL copper interconnects. Using these TVs, we experimentally determine the surface variation in the dielectric after spin coating, as a function of line heights, widths, and spacings, in addition to process variables. We model the resulting dielectric surface as a two-dimensional convolution between the underlying topography and an appropriately chosen impulse response (see Figure 1). The form of the impulse response is experimentally determined, and we predict the model coefficients based on the line height, coating thickness, and other process variables.

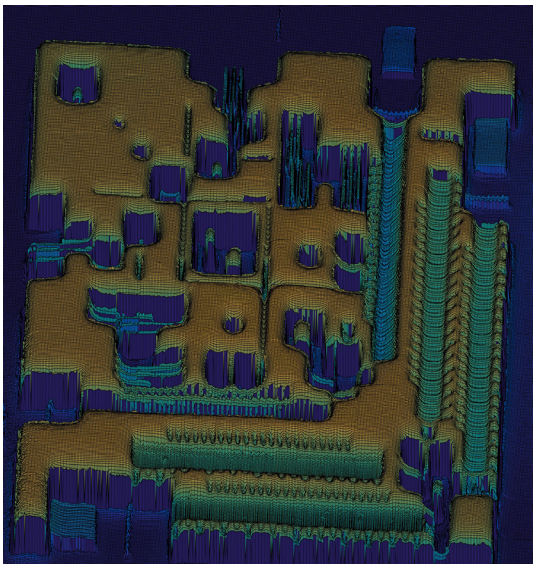

▲ Figure 1a: Experimental surface after spin coating.

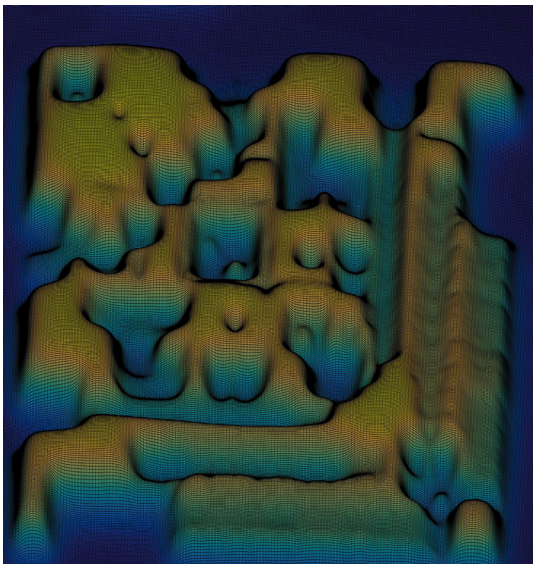

▲ Figure 1b: Predicted surface using 2D convolution model.

FURTHER READING

- L. E. Stillwagon and R. G. Larson, "Leveling of Thin Films Over Uneven Substrates During Spin Coating," *Physics of Fluids*, pp. 1937-1944, November 1990.

Tensor Recovery for Stochastic Simulation of Nanoscale Devices and Circuits with Many Process Variations

Z. Zhang, T.-W. Weng, L. Daniel
Sponsorship: NSF NEEDS, AIM Photonics

Process variations have become a "red-brick" problem that prevents the semiconductor industry progressing forward. A random fluctuation at the atomic scale can cause a large impact on the performance of nanoscale and device simulations. In order to increase chip yields, the uncertainties caused by process variations must be well estimated and controlled before a final fabrication. In traditional EDA tools, such a task is done by Monte Carlo-type simulators. Recently, stochastic spectral methods have emerged as a promising alternative. They are much more efficient than Monte Carlo simulators for certain design cases, but their efficiency can degrade as the number of process variations increases.

Our approach can efficiently handle design problems with 50 to 60 uncorrelated random parameters. We represent the huge number of device/circuit simulation samples in stochastic collocation by a tensor, which is a representation of a high-dimensional data array. Then, similar to the matrix case, we can exploit the low-rank structure of a tensor to reduce the storage and computational cost, as shown in Figure 1. Combining this low-rank property with the sparse property in high-dimensional generalized polynomial-chaos expansion, we have suggested a low-rank and sparse tensor recovery model. This optimization model allows us to estimate the huge number of unknown simulation samples based on a small number of available simulation results. Therefore, the computational cost can be reduced from an exponential one to a linear one.

This approach has been successfully applied to solve stochastic modeling and simulation problems in MEMS design and in CMOS IC design. For the CMOS ring oscillator with 57 uncorrelated process variations in Figure 2, stochastic collocation using a standard deterministic numerical integration requires 1.6E27 simulation samples, whereas our tensor recovery approach only needs 300 simulation samples to construct a highly accurate (with 1% relative error) stochastic model for the oscillator frequency.

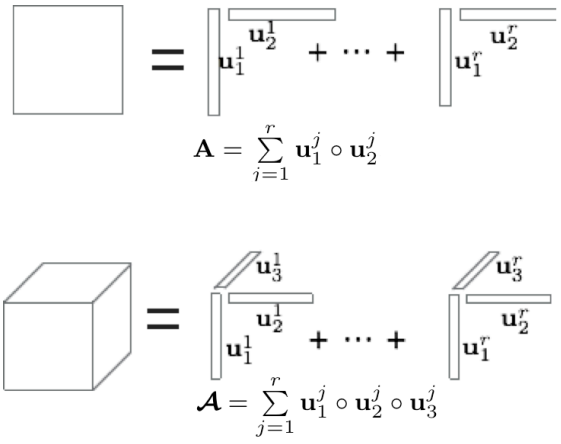

▲Figure 1: Low-rank decomposition of a matrix (top); and low-rank decomposition of a tensor (bottom). The low-rank decomposition allows representation of high-dimensional data arrays using a few vectors.

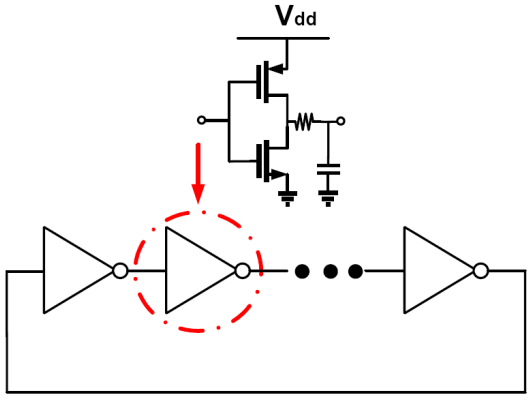

▲Figure 2: A CMOS ring oscillator. This circuit has 57 independent random parameters describing the variations of transistor threshold voltage, gate oxide thickness, channel length, and width.

FURTHER READING

- Z. Zhang, I. M. Elfadel, and L. Daniel, "Uncertainty Quantification for Integrated Circuits: Stochastic Spectral Methods," *Proc. Int. Conf. Computer-Aided Design*, pp. 803-810, 2013.
- Z. Zhang, T.-W. Weng, and L. Daniel, "A Big-Data Approach to Handle Process Variations: Uncertainty Quantification by Tensor Recovery," *Proc. IEEE Workshop on Signal and Power Integrity*, pp. 1-4, 2016.
- Z. Zhang, L. Daniel, K. Batselier, H. Liu, and N. Wong, "Tensor Computation: A New Framework for EDA," *IEEE Trans. CAD of Integrated Circuits and Systems*, submitted, 2016.

Chemical Sensors Based on GaAs Nanowires and oCVD Polymers

X. Wang, S. Ermez, H. Goktas, S. Gradečak, K. K. Gleason
Sponsorship: Shell

Room temperature gas sensing has always been an intriguing topic in the areas of oil industry, air condition monitoring, and healthcare. The motivation for a room temperature gas detector is that the traditional metal oxide sensor, although with a very high resistive response, requires high operational and manufacturing temperature. Our group has developed several types of room temperature gas sensors based on oxidative chemical vapor deposition (oCVD) polymers and nanostructures such as gold nanoparticles and aligned carbon nanotubes (A-CNT). Here we introduce a new chemical sensor based on GaAs nanowires and oCVD polymers. With a higher resistive signal than the CNT sensor and a lower noise than the polymer-Au nanoparticle sensor, this compact gas detector shows prospects for numerous applications.

The structure of the GaAs-oCVD sensor is comprised of a GaAs nanowire array and an oCVD coating layer. GaAs nanowire arrays with different density are grown via self-seeded nanowire growth mechanism using metal-organic chemical vapor deposition (MOCVD). A layer of oCVD polymer, usually a type of polythiophene, is further conformally coated on the GaAs nanowire arrays. Two metal electrodes are used to measure the resistive change after exposure to analytes. Our sensors show remarkable sensitivity to a variety of organic vapors with good selectivity. One potential application of this device could be a sensing element in a wireless sensor network with appropriate reading circuits.

FURTHER READING

- X. Wang, S. Hou, H. Goktas, P. Kovacik, F. Yaul, A. Paidimarri, N. Ickes, A. P. Chandrakasan, and K. K. Gleason. "Small-Area, Resistive Volatile Organic Compound (VOC) Sensors Using Metal–Polymer Hybrid Film Based on Oxidative Chemical Vapor Deposition (oCVD)," *ACS applied materials & interfaces* 7, no. 30, pp. 16213-16222, 2015.
- X. Wang, A. Ugur, H. Goktas, N. Chen, M. Wang, N. Lachman, E. Kalfon-Cohen, W. Fang, B. L. Wardle, and K. K. Gleason, "Room Temperature Resistive Volatile Organic Compound Sensing Materials Based on a Hybrid Structure of Vertically Aligned Carbon Nanotubes and Conformal oCVD/iCVD Polymer Coatings," *ACS Sensors* 1, no. 4, pp. 374-383, 2016.
- S. Ermez *et al*, "Self-seeded III-V Nanowire Growth by Metal-organic Chemical Vapor Deposition," *Crystal Growth and Design,* vol. 15, no. 6, pp. 2768–2774, 2015.

Cost-Effective and Scalable Sub-10 nm Patterning via Initiated Chemical Vapor Deposition

D. H. Kim, H. S. Suh, P. Moni, S. Xiong, L. E. Ocola, P. Nealey, K. K. Gleason
Sponsorship: NSF

Making smaller patterns in a cost-effective way has always challenged the semiconductor industries. The current 14-nm patterning process, commercially enabled by multiple photolithography, is reaching the limit in pattern resolution and manufacturing cost. Last year, the use of 7-nm patterns in a working chip by extreme ultraviolet (EUV) lithography with a wavelength of 13.5 nm was announced, but it remains in lab-scale because of its high-cost process and low productivity coming from the EUV light source. Directed self-assembly (DSA) has garnered great interest as a promising technology with no need to use such an expensive light source. The DSA enables control of the orientation and alignment of nanoscale domains of block copolymers (BCPs) thermodynamically for producing periodic nanostructures. However, the number of BCPs and the process window of DSA to permit sub-10-nm patterns are very limited by conventional spin coating.

Instead, we introduced initiated chemical vapor deposition (iCVD), a solvent-free process, to the DSA process for forming an effective topcoat on BCP (Figure 1). In iCVD, monomer and initiator vapors flow into a vacuum chamber. The resistively heated hot filaments in the chamber break the initiator into free radicals. Subsequently, polymeric film growth begins on cooled substrates through free-radical polymerization of monomer. Because iCVD is a solvent-free and low- temperature process, it is able to deposit polymeric films on fragile substrates such as polymers, papers, and textiles without affecting the substrates. These features of iCVD allow the scalable deposition of an ultrathin topcoat on a highly segregating (high χ) BCP for sub-10-nm patterning. During the thermal annealing of DSA, the iCVD topcoat inhibits the collapse of the perpendicular orientation of BCP domains completely and then generates sub-10-nm line and space patterns underneath the iCVD topcoat. As a result, the iCVD topcoat creates sub-10-nm patterns from chemical guide strips of DSA with relatively low resolution patterns (pitch: ~40 nm), as seen in Figure 2. Spectroscopic studies reveal that iCVD forms the unique interface between BCPs and the topcoat, which is a mixed interface made by grafting and intermolecular entanglements. This unusual interface is not observed in a spun-cast topcoat.

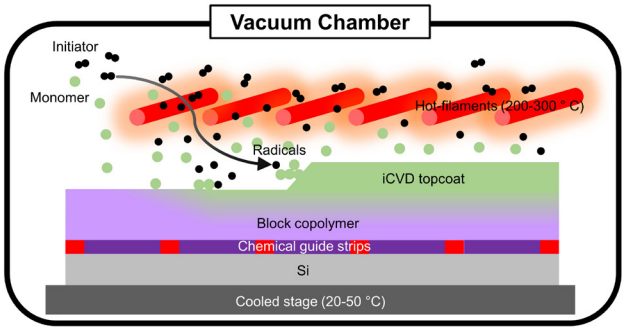

▲Figure 1: The iCVD process to deposit a polymeric topcoat on block copolymers for creating sub-10-nm patterns in conjunction with DSA.

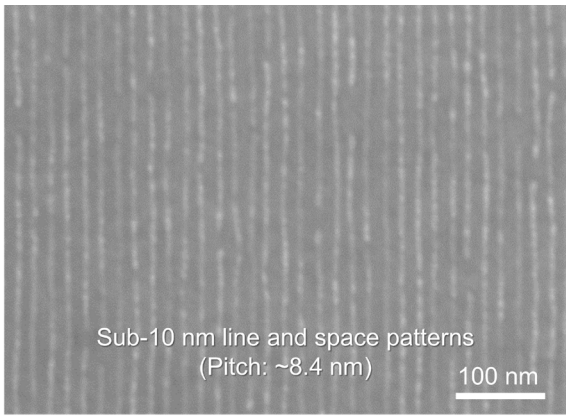

▲Figure 2: Scanning electron microscopic images taken from sub-10-nm line and space patterns with a pitch, ~8.4 nm underneath iCVD topcoat. The scale bars are 100 nm.

FURTHER READING

- O. Kim, H. H. Solak, M. P. Stoykovich, N. J. Ferrier, J. J. de Pablo, and P. F. Nealey, "Epitaxial Self-assembly of Block Copolymers on Lithographically Defined Nanopatterned Substrates," *Nature*, vol. 424, pp. 411–414, 2003.
- J. L. Yagüe, A. M. Coclite, C. Petruczok, and K. K. Gleason, "Chemical Vapor Deposition for Solvent-Free Polymerization at Surfaces," *Macromol. Chem. Phys.* vol. 214, pp. 302–312, 2013.

Free-standing Nano-Gratings as Phase-Shifting Devices for Electron Optics

Y. Yang, R. G. Hobbs, C.-S. Kim, K. K. Berggren
Sponsorship: Gordon and Betty Moore Foundation

Nanofabricated phase-shifting devices for electron optics are of interest for a variety of applications, such as beam splitters for electron interferometry and holography, holograms for electron vortex beam generation, and phase plates for contrast enhancement in electron microscopy. Nano-fabricated gratings provide more flexible control of diffraction angle and orbital angular momentum of diffracted electron beams compared to crystalline electron diffraction "gratings" and can be used at a variety of electron energies. For the applications given above, it is crucial to understand shifts in the phase of the electron beam imposed by these phase-shifting devices. Here we report a nanofabricated two-dimensional transmission grating for electron beams and its characterization with electron diffraction in a transmission electron microscope (TEM) at various electron energies.

The electron transmission gratings were fabricated from silicon nitride membrane (5-10 nm) TEM grids (*SiMPore Inc.*).High-resolution electron beam lithography (EBL) was used to define the grating pattern. After resist development, pattern transfer to the silicon nitride membrane was achieved with reactive-ion etching (RIE). Finally, the silicon nitride gratings were coated with approximately 10 nm of metal (gold or aluminum) to prevent charging in the experiment. Nano-gratings were characterized in a FEI Tecnai TEM in selected-area diffraction mode (Figure 1(a)). The electron energy was varied from 120 keV to 40 keV so that the membrane imposed different phase shifts to the electron beam, hence modulating the intensities of diffracted beams. The electron beam phase shifts were estimated by fitting experimentally measured intensities of diffracted beams to theoretical calculations. It was found that the membrane imposed the same phase shift as that of a 40-nm-thick membrane made of a material with a 20-V mean inner potential. The phase shift was found to be 2.2-3.5π for electrons with 120-40 keV energy.

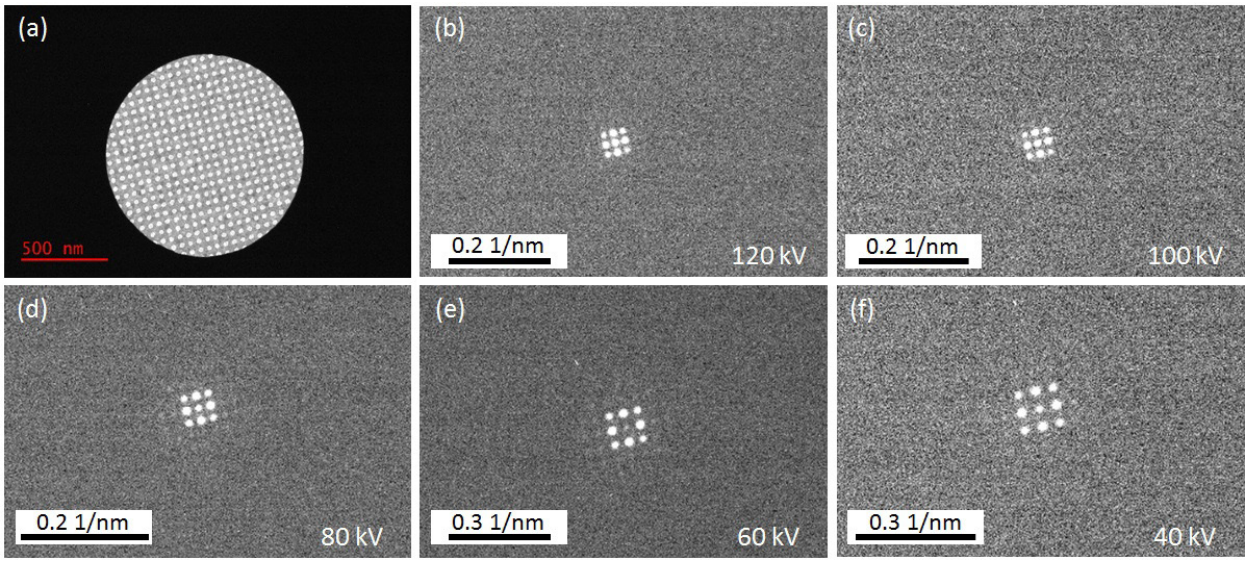

▲ Figure 1: Selected area TEM image and electron diffraction patterns of a nanofabricated transmission grating. (a) A two-dimensional mesh grating patterned from a 10-nm-thick silicon nitride membrane by EBL and RIE, followed by 10-nm gold coating to prevent charging during imaging and diffraction. The grating pitch is 50 nm. A selected area aperture is inserted to select a circular area with ~ 1-μm diameter. (b-f) Selected-area electron diffraction patterns from the mesh grating shown in (a), with electron energies from 120 keV to 40 keV. The TEM acceleration voltages are labeled. The diffract patterns are taken with a large camera length (4.8 m) to zoom into the center beam, while relatively high-angle electron diffraction from polycrystalline gold is not shown.

FURTHER READING

- J. Verbeeck, H. Tian, and P. Schattschneider, "Production and Application of Electron Vortex Beams," *Nature*, vol. 467, pp. 301-304, 2010.
- G. Gronniger, B. Barwick, H. Batelaan, T. Savas, D. Pritchard, and A. Cronin, "Electron Diffraction from Free-Standing, Metal-Coated Transmission Gratings," *Applied Physics Letters*, vol. 87, pp. 124104, 2005.
- P. Kruit, R. G. Hobbs, C-S. Kim, Y. Yang, V. R. Manfrinato, J. Hammer, S. Thomas, P. Weber, B. Klopfer, C. Kohstall, T. Juffmann, M. A. Kasevich, P. Hommelhoff, and K. K. Berggren, "Designs for a Quantum Electron Microscope," *Ultramicroscopy*, vol. 164, pp. 31-45, 2016.

Scanning Electron Microscopy with a Reflected Electron Beam

N. Abedzadeh, R. G. Hobbs, C.-S. Kim, K. K. Berggren
Sponsorship: Gordon and Betty Moore Foundation

Although electron microscopy has enabled imaging of biological specimens with near-atomic scale resolution, the damage that the electron beam imparts to these samples has been an unavoidable disadvantage that still limits the scope and throughput of the technique. Interaction-free measurement using a quantum electron microscope (QEM) is a scheme proposed to reduce or eliminate damage to biological samples. One possible path to realization of a QEM is to construct an electron resonator like that shown in Figure 1, including a diffractive electron optic such as a grating mirror in which Mach Zehnder-type splitting and re-coupling occur between the zero-order and first-order diffracted beams.

This project was broken into two sub-tasks: 1) design and construction of an electron mirror enabling simultaneous imaging of both the upper and underside of a sample with an electron beam, and 2) design and fabrication of a reflective diffraction grating for electrons, whereby a potential equivalent to the electron energy is applied to the grating. The diffraction grating functions both as the mirror and as the element that splits and re-couples the diffracted beams (see Figure 1). Finally, we will characterize diffraction from the grating by obtaining multiple images of the underside of a sample using zero-order and first-order diffracted beams.

Figure 2 shows the first demonstration of simultaneous imaging of the top and bottom surfaces of a sample in a SEM with a flat, unpatterned mirror surface. Figure 2 (a) shows that after the voltage applied to the mirror and lens system is tuned, the incident electron beam scans the top surface while the reflected beam scans the underside of the sample, resulting in the image shown in Figure 2 (b). The resolution of the reflected image is currently limited by the long working distance used in the SEM and astigmatism induced by the lens and mirror setup. The next step in this project is to reduce the working distance by rearranging the system configuration and to repeat the experiment with a grating mirror.

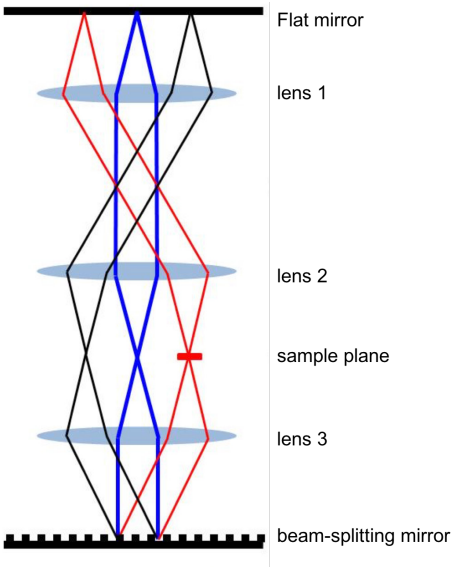

▲Figure 1: Schematic representation of the electron cavity considered for the QEM: diffractive mirror approach with grating mirror.

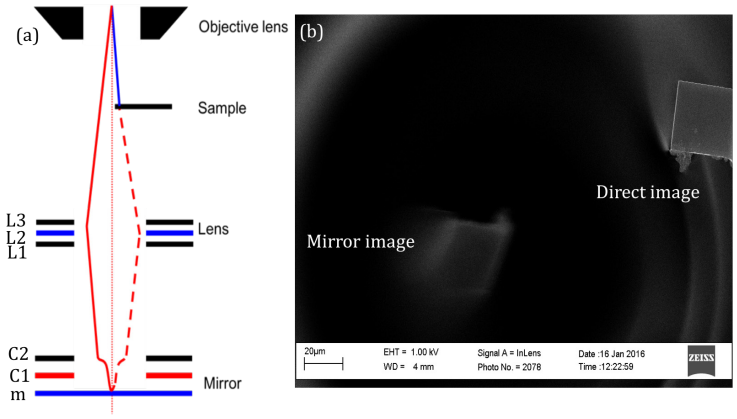

▲Figure 2: (a) Schematic of setup used to image top and bottom surfaces of a sample simultaneously. Voltages applied to electrodes from bottom to top: V_m=-1050 V, V_{c1}=+6095 V, V_{c2}=0 V, V_{L1}=0 V, V_{L2}=-800 V, and V_{L3}=0 V. Energy of incident electron: 1 keV. (b) SEM image of top and bottom surfaces of a sample simultaneously using the in-lens secondary electron detector. The scale bar is 20 µm.

FURTHER READING

- W. P. Putnam and M. Fatih Yanik, "Noninvasive Electron Microscopy with Interaction-free Quantum Measurements," *Physical Review A*, vol. 80, pp. 040902, October 2009.
- P. Kruit, R. G. Hobbs, C-S. Kim, Y. Yang, V. R. Manfrinato, J. Hammer, S. Thomas, P. Weber, B. Klopfer, C. Kohstall, T. Juffmann, M. A. Kasevich, P. Hommelhoff, and K. K. Berggren, "Designs for a Quantum Electron Microscope," *Ultramicroscopy*, vol. 164, pp. 31-45, March 2016.

A Microfabricated Mach-Zehnder Interferometer for Electrons

A. Agarwal, C-S. Kim, R. G. Hobbs, D. Van Dyck, K. K. Berggren
Sponsorship: Gordon and Betty Moore Foundation

Electron interferometers, necessary for electron holographic microscopy, are usually constructed with a biprism as the beamsplitter. Interferometers that use diffraction from crystalline or nanofabricated gratings to split and recombine the beam offer the possibility of interferometry in a standard scanning electron/transmission electron microscope (SEM/TEM) but require precise and difficult alignment of the position and orientation of the gratings. To address this challenge, we designed an interferometer for a TEM based on a monolithic three-crystal grating fabricated by focused ion-beam milling of a single crystal of silicon, as shown in Figure 1(a).

We used parallel- and convergent-beam electron diffraction (PBED and CBED) to characterize the gratings. In PBED, diffraction spots arising from the first and second crystals overlap in the back focal plane, thus proving that the gratings are well aligned (Figure 1(b)). CBED yields a diffraction pattern with an array of satellite spots, as shown in Figure 1(c). Unlike conventional CBED, which looks at disks at or close to the back focal plane, we focused the diffraction pattern by controlling the intermediate lens (IL) and moving to the second crossover plane, where the diffracted beams from the first and second crystals are focused at horizontally displaced spots. We can build up the experimental pattern from Figure 1(c) by taking all diffraction orders into account.

We also fabricated a three-crystal grating with 23-μm separation between the crystals (Figure 2) to ensure that the first-order diffracted beam from the first crystal separates from the zero-order beam in the plane of the second crystal; this gives two independent arms of the Mach-Zehnder interferometer (drawn schematically in Figure 2). We imaged the beam separation on the second crystal and overlap on the third (Figure 2), but dynamical diffraction effects obscured the expected interference fringes. We are optimizing our design parameters (beam convergence angle, grating separation) to minimize these effects.

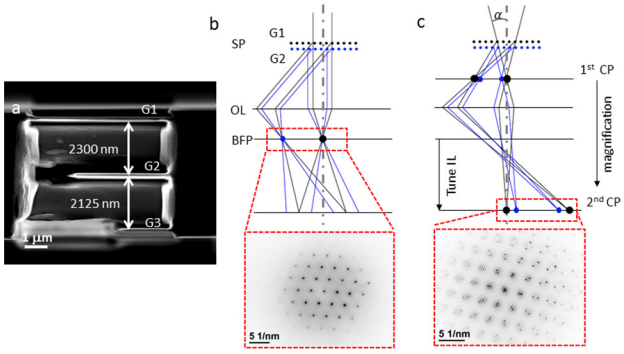

▲ Figure 1: (a) Monolithic three-crystal grating fabricated from Si (110) by FIB. (b) Ray diagrams and experimentally observed DPs for PBED and (c) CBED. Black and blue rays represent diffraction from G1 and G2, respectively. (G1: first grating, G2: second grating, SP: sample plane, OL: objective lens, BFP: back focal plane, CP: crossover plane, α: convergent angle).

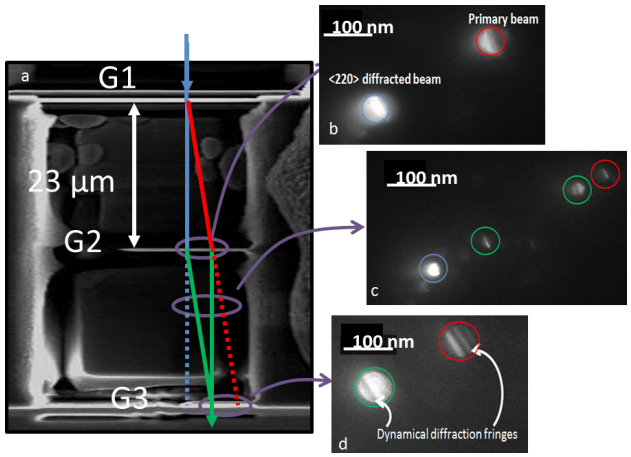

▲ Figure 2: (a) 23-μm separation multi-grating with schematic of a Mach-Zehnder interferometer. First grating splits incident electron beam into primary and diffracted beam, which are recombined by second grating. By tilting sample holder so that grating is in 2-beam condition and varying objective lens current to change imaging plane, we imaged beam (b) in plane of second, (c) between second and third and (d) on third crystal, demonstrating beamsplitting and recombination.

FURTHER READING

- L. Marton, J. A. Simpson and J. A. Suddeth, "Electron Beam Interferometer," *Phys. Rev.* vol. 90, pp. 490, 1953.
- G. Gronniger, B. Barwick and H. Batelaan, "A Three-grating Electron Interferometer," *New Journal of Physics*, vol. 8, pp. 224, 2006.

Lithographically Patterned Nanostructures for Geometric Control of Coiled-Coil Protein Placement and Alignment

M. Bedewy, W. M. Park, A. E. Keating, K. K. Berggren
Sponsorship: DuPont

Developing methods to tailor nanoscale surface features has received significant attention recently, in particular for applications requiring control of living cell behavior. Engineering nanoridges to regulate cells in cardiac tissue constructs or using nanotubes to direct growth of motor neuron cells are two examples. Although various nanofabrication methods are capable of producing surfaces with anisotropic structure and properties at the nanoscale, most of these nanoengineered surfaces are made of synthetic and non-organic materials that are not necessarily biocompatible. Moreover, engineered surfaces do not mimic the atomic scale morphology and interactions of the native protein-based environment of the extracellular matrix. Hence, controlled functionalization of nanostructured surfaces with proteins is desired for advanced biointerfaces. While block copolymer micelle nanolithography and scanning probe methods have been used for this purpose, they are limited to spherical nanoparticles and randomly oriented protein binding.

In this work, we used electron beam lithography (EBL) to create arrays of designed nanoscale feature geometries and pattern topologies down to the 10-nm scale. Patterns are transferred to gold by deposition and lift-off. Silicon substrates are functionalized with a monolayer of methoxy polyethylene glycol (PEG) silane to prevent the nonspecific binding of proteins on non-patterned areas of the substrate. Purified coiled-coil tropomyosin proteins are then selectively immobilized on the surface by leveraging the formation of a thiol bond between the cysteine group at one end of the protein and the lithographically patterned gold. Atomic force microscopy was used to assess the protein structure and location, and scanning electron microscopy was also used to characterize the surface, after proteins were tagged with Au nanoprobes. Combining the versatility of EBL and the specificity of bottom-up protein binding makes this approach attractive for scalable production of nanobiointerfaces in high-sensitivity medical diagnostics and regenerative medicine.

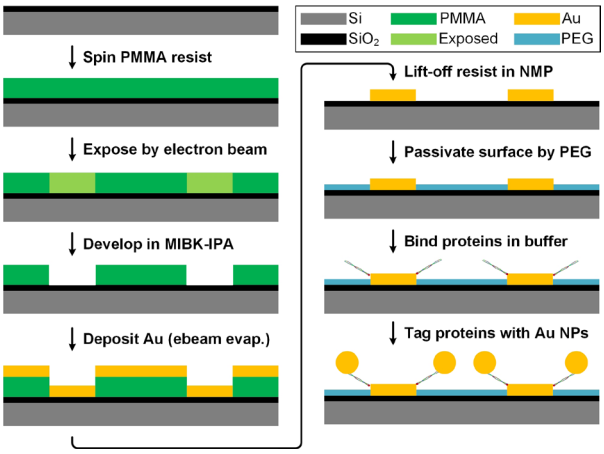

▲Figure 1: Process schematic showing fabrication of gold nanostructures by EBL and lift-off and attaching of PEG silane. Samples are incubated with proteins in buffer and in solution with gold nanoprobes for protein tagging.

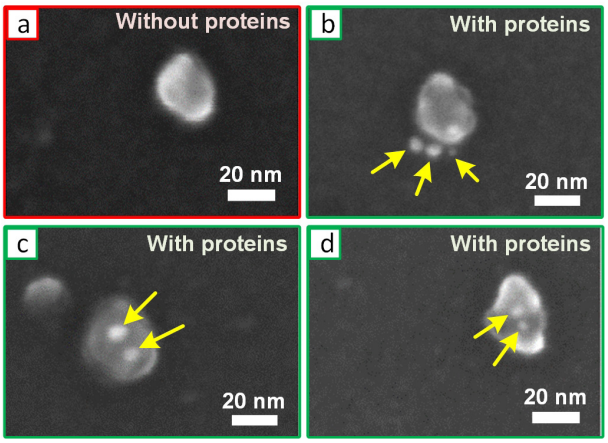

▲Figure 2: Scanning electron micrographs showing initial results for protein localization on 20-nm gold posts created by EBL. (a) gold nanopost without proteins. (b-d) gold nanoposts with proteins and nanoparticle tags.

FURTHER READING

- J.-B Chang, Y. H. Kim, E. Thompson, Y. H. No, N. H. Kim, J. Arrieta, V. R. Manfrinato, A. E. Keating, and K. K. Berggren, "The Orientations of Large Aspect-Ratio Coiled-Coil Proteins Attached to Gold Nanostructures," *Small*, vol. 12, pp. 1498–1505, 2016.
- A. W. Reinke, R. A. Grant, and A. E. Keating, "A Synthetic Coiled-Coil Interactome Provides Heterospecific Modules for Molecular Engineering," *Journal of Am. Chem. Soc.* vol. 132, pp. 6025-6031, 2010.
- V. R. Manfrinato, L. Zhang, D. Su, H. Duan, R. G. Hobbs, E. A. Stach, and K. K. Berggren, "Resolution Limits of Electron-Beam Lithography Toward the Atomic Scale," *Nano Letters*, vol. 13, pp. 1555-1558, 2013.

Multidirectional Block Copolymer Alignment: Shear-Induced Alignment by Mismatch of Thermal Coefficients of Expansion

S. M. Nicaise, A. Tavakkoli K. G., K. GadelraA. Alfredo-Katz, C. A. Ross, K. K. Berggren
Sponsorship: TSMC

Here we show shear-aligned BCP cylinders induced by a SiO_2 top-coat. The fabrication process involves four steps: (1) spin-coating a thin film of cylinder-forming BCP, poly(styrene-*b*-dimethylsiloxane) (PS-*b*-PDMS, 16 kg mol^{-1}) on Si; (2) deposition of ~100 nm of SiO_2 on the BCP; (3) thermal annealing of samples for 1 and 10 minutes, inducing oriented assembly; and (4) SiO_2 removal in 1% hydrofluoric acid and reactive-ion etching to leave PDMS cylinders. During annealing, the SiO_2 (coefficient of thermal expansion (CTE) ~0.5 ppm/°C) expanded less than the silicon (CTE ~2.6 ppm/°C). The resulting strain aligned the BCP cylinders perpendicular to scribes and cracks in the SiO_2.

The degree of alignment varied with annealing temperature and distance from hand-scribes. In Figure 1, we plotted the greatest distance from the scribe for which we observed ordering and alignment. BCP ordering increased with proximity to the crack, likely due to higher shear-stress at the SiO_2 free edge, as determined via finite-element simulation of the BCP-SiO_2 and –Si interfaces. Longer annealing time and higher annealing temperature resulted in improved long-range alignment and reduced defects. Furthermore, rapid orientation was achieved in as little as one minute of annealing. Different BCP orientations were achieved using crossed hand-scribes (Figure 2). Overall, this method shows promise to improve local orientational control as well as the long-range order of BCPs.

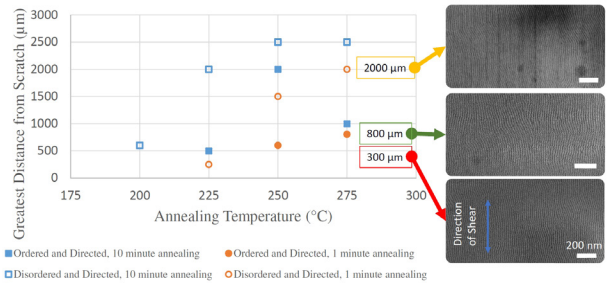

▲ Figure 1: Maximum observed distance (away from scribe) of ordering and direction vs. annealing temperature and time. Also, example scanning-electron micrographs of the aligned BCP at chosen distances.

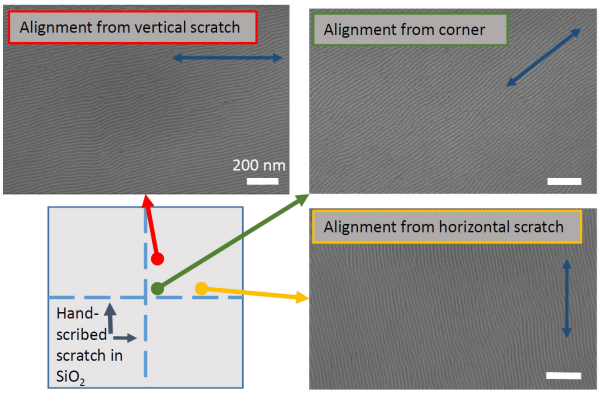

▲ Figure 2: The cartoon shows a cross hand-scribed in the SiO_2. The scanning electron micrographs show controlled shear-aligned BCP cylinders in directions perpendicular to the scribes on a single substrate.

FURTHER READING

- D. E. Angelescu, J. H. Waller, D. H. Adamson, P. Deshpande, S. Y. Chou, R. A. Register, and P. A. Chaikin, "Macroscopic Orientation of Block Copolymer Cylinders in Single-Layer Films by Shearing," *Advanced Materials*, vol. 16, pp. 1736-1740, 2004.
- Z. Qiang, L. Zhang, G. E. Stein, K. A. Cavicchi, and B. D. Vogt, "Unidirectional Alignment of Block Copolymer Films Induced by Expansion of a Permeable Elastomer during Solvent Vapor Annealing," *Macromolecules*, vol. 47, pp. 1109-1116, 2014.
- J. W. Eischen, C. Chung, and J. H. Kim, "Realistic Modeling of Edge Effect Stresses in Bimaterial Elements," *Trans. ASME*, vol. 112, pp. 16-23, 1990.

Rule-Based Patterning of a Multi-State System by Block Copolymer Self-Assembly

H. Do, H. Choi, J.-B. Chang, C. A. Ross, K. K. Berggren
Sponsorship: NSF, Taiwan Semiconductor Manufacturing Company

Lithographic confinement can direct the self-assembly of block copolymers (BCPs) to achieve highly ordered nanoscale patterns. Previously, we have demonstrated that BCP cylinders can form a multi-state system with ladder-shaped structures rather than a single-state system with concentric rings inside a confinement when the bending angle of the confinement is 90° or more. In this work, we describe a design rule to determine the individual state of the ladder-shaped structures by controlling alignment direction. This work could lead to a new patterning method that enables higher-throughput pattern generation.

We fabricated topographic templates consisting of square cells with one to four openings using electron-beam lithography of hydrogen silesquioxane resist. Figure 1 shows five different types of the square confinements and the measured probability of horizontal alignment, denoted as the 0 state. The templates were chemically functionalized with a hydroxyl-terminated polystyrene brush. Next, 45.5 kg/mol polystyrene-*b*-polydimethylsiloxane BCP (PS-*b*-PDMS) was spin cast on the templated substrate, and the sample was solvent annealed using a 5:1 mixture of toluene and heptane at room temperature for 5 h. The upper PDMS layer and PS matrix were removed using CF_4 and O_2 plasma treatment, respectively. Templates without openings produced ladder-shaped BCP patterns inside the square cell with equal probability of horizontal and vertical alignment. When one or more openings were introduced, the alignment directions were controlled by a majority rule determined by the number of horizontal and vertical openings.

Using five design rules, we fabricated an array of connected binary states where the two states were defined as horizontally (0 state) and vertically (1 state) aligned structures. Two examples of complex 4 by 4 binary patterns each composed of 16 independently controlled binary states are shown in Figure 2. After BCP self-assembly, binary states formed inside the template matched the desired binary patterns.

In the future, the possibility of propagating template information across multiple tiles will be investigated.

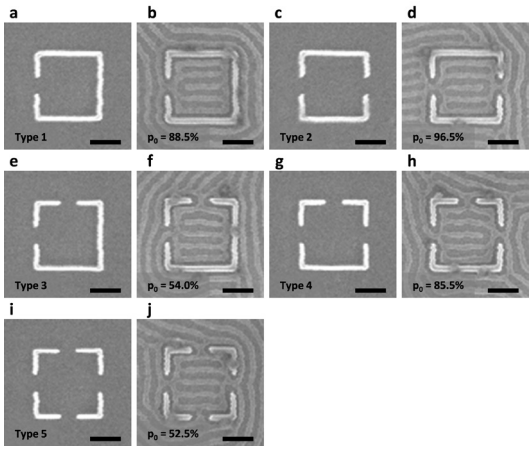

▲Figure 1: Scanning electron microscope images of square confinement with different number of openings and resulting block copolymer patterns. Probability of horizontal alignment (0 state) for each type was measured. Binary states were determined by a design rule based on majority rule. Scale bars, 200 nm.

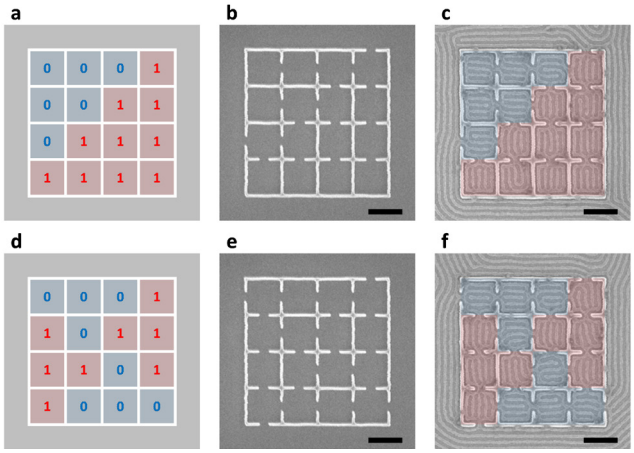

▲Figure 2: Fabrication of binary state arrays. (a, d) Diagram of desired 4 x 4 binary state arrays. (e) Templates fabricated by rule-based design. (c, f) Resulting block copolymer patterns matching the desired binary states. Red indicates 0 state, and blue indicates 1 state. Scale bars, 200 nm.

FURTHER READING

- J. Y. Cheng, A. M. Mayes, and C. A. Ross, "Nanostructure Engineering by Templated Self-assembly of Block Copolymers," *Nature*, vol. 3, pp. 823-828, 2004.

Mapping Deep-Ultraviolet Plasmons in Lithographically Defined Aluminum Nanostructures

S. A. Goodman, R. G. Hobbs, V. R. Manfrinato, Y. Yang, L. Zhang, E. A. Stach, K. K. Berggren
Sponsorship: Gordon and Betty Moore Foundation, DOE EFRC

An electron beam induces collective oscillations of the free-electron gas in a material that take the form of surface plasmons (SPs) or volume plasmons (VPs). SPs are transverse and propagate at the material surface whereas VPs are longitudinal and propagate in the bulk of the material. Due to their longitudinal nature, VPs do not couple to light and must be excited by charged particle beams. Here, we demonstrate nanometer-scale mapping of SP and VP modes across these nanostructures using spatially resolved electron energy loss spectroscopy (EELS) with a scanning transmission electron microscope (STEM). Figure 1a shows a high-angle annular dark field STEM image of a 12-nm-diameter Al nanodisk. To create an EELS map of this nanodisk, a focused electron beam with a sub-nanometer-sized probe is raster-scanned across the sample (Figure 1b). Electrons passing through the material undergo various energy-loss pathways including plasmon excitation. An EEL spectrum (Figure 1c) is recorded at each 1-nm^2 pixel; the spectrum represents the number of electrons plotted versus energy-loss and contains Al SP peaks (2-8 eV), the Al VP peak (15 eV), and the Al_2O_3 VP peak (23 eV). Figure 1d shows three superimposed EELS maps obtained at each plasmon energy, providing a nanometer-scale representation of the local electric field density across the nanodisk. As demonstrated by the EELS map and plasmon intensity profile (Figure 1e), the Al VP mode is localized at the center of the particle while the Al SP mode is localized at the particle boundary. With SP resonances that can be tuned from the visible to the UV and a VP resonance in the deep-UV, Al is a promising material for high-energy plasmonics. The ability to map the spatial distribution of plasmon modes in Al nanodisks opens up a pathway for new optics, emitters, and hot-carrier-based chemistry in the UV range.

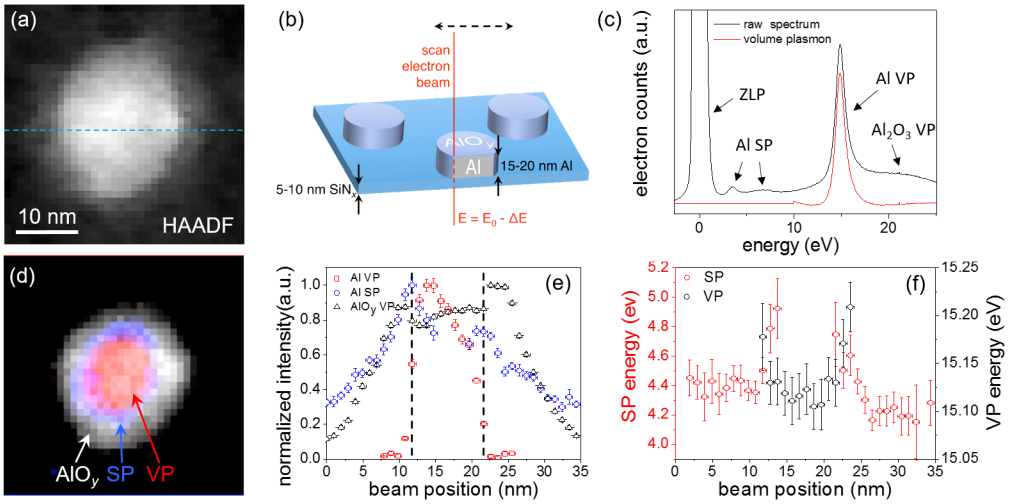

▲ Figure 1: EELS mapping of plasmon modes. (a) High-angle annular dark-field image of 12-nm-diameter Al nanodisk fabricated on 5-nm-thick SiN_x TEM grid. Scale bar also applies to (d). Blue dashed line represents path of electron beam in (e, f). Images and EEL spectra were acquired on aberration-corrected Hitachi HD2700C STEM at Brookhaven National Lab. (b) Electron beam is raster scanned across nanodisk, and EEL spectrum is recorded at each pixel. (c) Example EEL spectrum representing number of electrons vs. energy loss. Raw spectrum contains zero loss peak (ZLP), Al SP peaks, Al VP peak, and VP peak of Al_2O_3. Background is subtracted to obtain isolated Al VP peak (in red). (d) Superposition of three EELS maps acquired at energy of Al dipolar SP1, Al VP, and Al_2O_3 VP. (e) Normalized SP1 and VP intensities plotted as function of electron beam position. Dashed lines show two SP1 maxima, indicating position of particle boundary. (f) Energy of SP1 and VP modes vs. beam position.

FURTHER READING

- R. H. Ritchie, R. Hamm, J. Turner, H. Wright, J. Ashley, and G. Banks, "Physical Aspects of Charged Particle Track Structure," *US Department of Energy Publications*, January 1989.
- R. H. Ritchie, "Plasma Losses by Fast Electrons in Thin Films," *Phys. Rev.*, vol. 106, no. 5, pp. 874–881, June 1957.
- R. G. Hobbs, V. R. Manfrinato, Y. Yang, S. A. Goodman, L. Zhang, E. A. Stach, and K. K. Berggren, "High-Energy Surface and Volume Plasmons in Nanopatterned Sub-10 nm Aluminum Nanostructures," *Nano Letters*, vol. 16, no. 7, pp. 4149-4157, July 2016.

Bias-Sputtered Few-Nanometer-Thick Niobium Nitride for Superconducting Devices

A. Dane, A. McCaughan, D. Zhu, Q. Zhao, C-S. Kim, N. Calandri, F. Bellei, K. K. Berggren
Sponsorship: NASA Space Technology Research Fellowship

Few-nanometer-thick films of low temperature superconducting materials have become increasingly important for sensitive photonic devices. Hot electron bolometers, superconducting nanowire single photon detectors (SNSPDs), microwave kinetic inductance detectors, and transition edge sensors are all broadband, highly sensitive photo-detectors that are fabricated from thin films of low-temperature superconducting materials.

Improvements to materials synthesis and exploration of material-dependent properties of these devices have so far taken a back seat to advancing the performance of individual devices through electrical design. In particular, while the performance of individual few-nanometer-thick niobium nitride (NbN) SNSPDs has produced detectors with near-unity quantum efficiency and tens of picoseconds of jitter, the yield of these devices remains a major issue. As optical systems demand longer nanowire devices and arrays of devices, previously ignored yield issues must be addressed.

We have explored reactive DC magnetron sputtering of few-nanometer-thick NbN without intentional substrate heating and the performance of superconducting devices made from NbN. We find that for films with thicknesses typical of those used to fabricate SNSPDs, the addition of a 50 watt substrate bias and the ion bombardment that results during film deposition significantly reduce the film resistivity, increase the Tc, decrease the film roughness, and change the film's surface morphology. This material shows promise for fabricating SNSPDs with better yield and efficiency at easy-to-access temperatures. Many fabrication methods and structures become practical when the substrate is not heated.

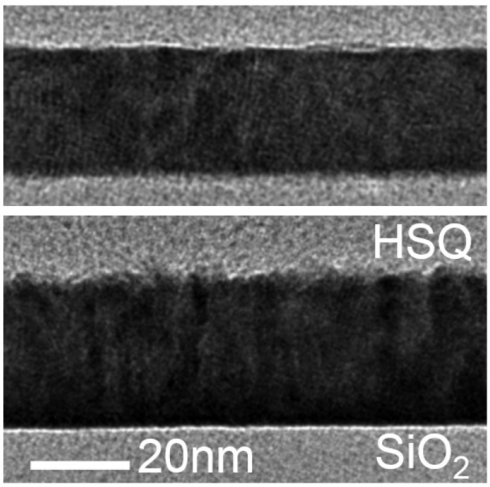

▲ Figure 1: Transmission electron microscope image of ~30-nm-thick NbN deposited by reactive magnetron sputter deposition without intentional heating. During the deposition a 50-watt RF bias was used to encourage ion bombardment and surface diffusion for the film shown on top.

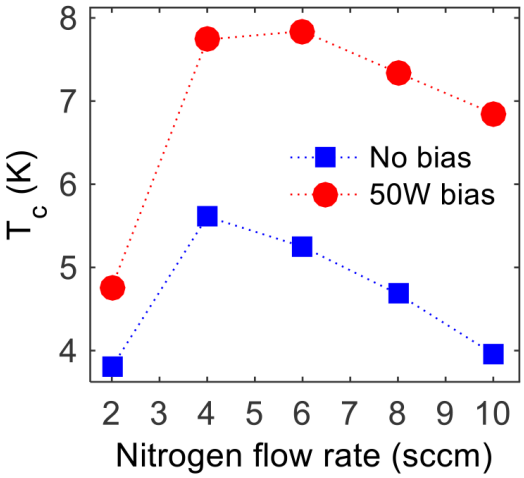

▲ Figure 2: The addition of a 50-watt RF bias increases the superconducting critical temperature of 5-nm- thick NbN films for different chamber conditions. The maximum T_c is seen to increase by about 2K.

FURTHER READING

- A. J. Kerman, E. A. Dauler, J. K. W. Yang, K. M. Rosfjord, V. Anant, K. K. Berggren, G. N. Gol'tsman, and B. M. Voronov, "Constriction-limited Detection Efficiency of Superconducting Nanowire Single-photon Detectors," *Appl. Phys. Letters*, vol. 90, no. 10, pp. 101110, 2007.
- L. Kang, B. B. Jin, X. Y. Liu, X. Q. Jia, J. Chen, Z. M. Ji, W. W. Xu, P. H. Wu, S. B. Mi, A. Pimenov, Y. J. Wu, and B. G. Wang, "Suppression of Superconductivity in Epitaxial NbN Ultrathin Films," *Journal of Appl. Phys.*, vol. 109, no. 3, pp. 033908, 2011.

Freeform Robotic Stereolithography

A. G. Stevens*, C. R. Oliver*, M. Kirchmeyer, J. Wu, L. Chin, E. S. Polsen, C. Archer, C. Boyle, J. Garber, A. J. Hart
*authors contributed equally
Sponsorship: NSF, SMART

Additive manufacturing by layerwise photopolymerization, i.e., sterolithography, is attractive due to its high resolution and diversity of materials chemistry; however, traditional stereolithography methods are restricted to planar substrates and single-axis machine configurations. We present a robotic system capable of maskless layerwise photopolymerization on curved surfaces, enabling production of large-area conformal patterns and the construction of freeform objects. The system comprises an industrial six-axis robot and a custom-built maskless projector end-effector. Use of the system involves scanning the freeform substrate, generation of a triangulated toolpath with curved layers that represents the target object to be printed, precision mounting of the substrate in the robot workspace, and robotic photopatterning of the target object by coordinated motion of the robot and substrate. We demonstrate printing of conformal patterns on spheres of various sizes, and construction of miniature three-dimensional objects without requiring support features (Figure 1). Improvement of the motion accuracy and development of freeform tool paths could enable construction of large polymer parts beyond the size and support structure constraints of traditional stereolithography systems

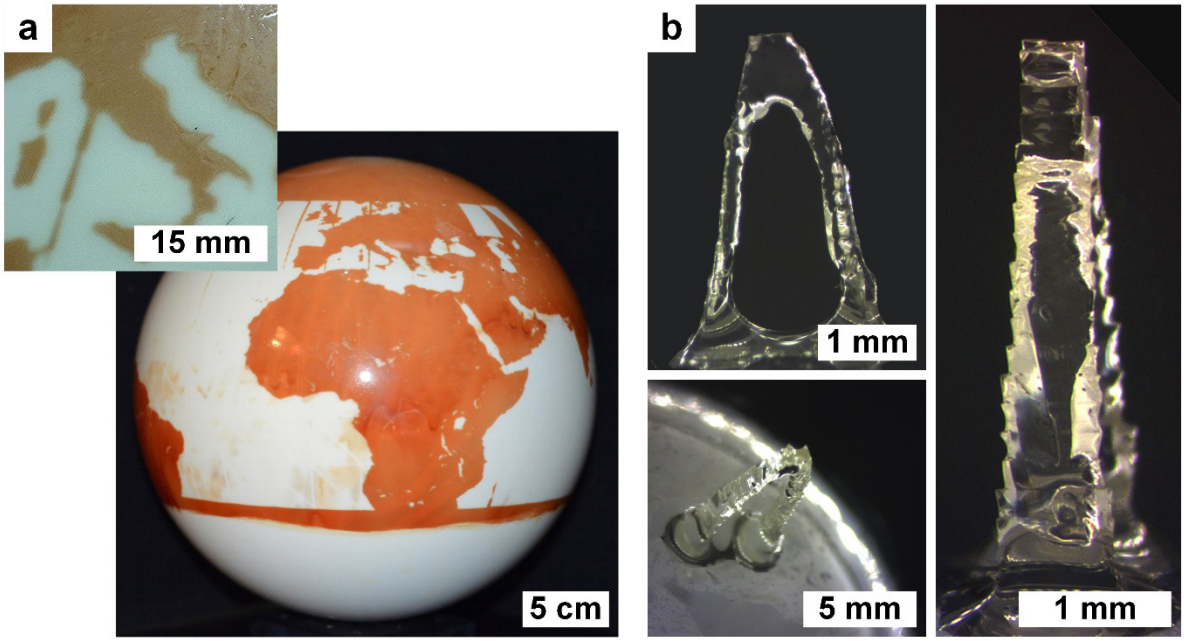

▲ Figure 1: Demonstrations of robotic stereolithography: (a) conformal patterning of photoresist (orange) on a spherical substrate (white); (b) miniature arch printed via robotic stereolithography (200-μm layers) on a spherical substrate.

FURTHER READING

- A. G. Stevens, C. R. Oliver, M. Kirchmeyer, J. Wu, L. Chin, E. Polsen, C. Archer, C. Boyle, J. Garber, and A. J. Hart, "Freeform Robotic Stereolithography," submitted for publication.

Measuring Phonon Mean Free Path Distributions in Materials via Quasiballistic Thermal Transport by Using Grating Nanostructures

L. Zeng, R. He, D. Wang, S. Huberman, V. Chiloyan, Z. Ren, G. Chen
Sponsorship: S3TEC, DOE

Thermal transport in non-metals generally consists of contributions from phonons spanning a wide range of mean free paths (MFPs). Knowledge of phonon MFP distributions is important for both fundamental understanding of microscopic energy transport in materials and many technological applications, including thermal management in microelectronics and thermal conductivity engineering in thermoelectric energy conversion. The thermal conductivity accumulation function is a key metric that describes the distribution of phonon MFPs that contribute to heat transport. To gain insight into materials' MFP distributions, the Nanoengineering Laboratory in the Department of Mechanical Engineering at MIT has been developing thermal conductivity spectroscopy techniques by utilizing a femtosecond ultrafast pump-probe setup.

The key idea of reconstructing material's MFP distribution is based upon combining experimental observation of quasiballistic thermal transport and solution of the phonon Boltzmann transport equation. Accessing the quasiballistic transport regime requires creating characteristic heater sizes comparable with the phonon MFPs. Since phonon MFPs in many materials of interest span from nanometers to micrometers, we lithographically patterned 2D metallic nanodots on top of the sample to function as both heat absorbers and temperature transducers during measurement. To avoid direct photo-excitation in opaque samples, we used a bilayer hybrid nanostructure to effectively localize the heating with nanometer scale resolution while preventing laser transmission into the substrate. Using this hybrid nanostructure approach, we studied length-dependent thermal transport in many materials, including Si, GaAs, GaN, and SiGe, and developed techniques to map out their intrinsic phonon MFP distributions. We then simplified the hybrid approach by utilizing 1D metallic wire grid polarizers to minimize carrier excitation in the substrate. At present, we are applying the simplified technique to measure MFP distributions in a range of materials, including some select thermoelectric materials. The measurement results will shed light on how to further tailor the thermal conductivity for energy applications.

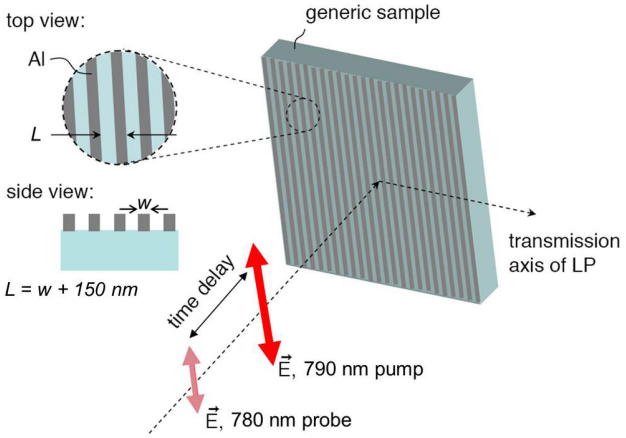

▲ Figure 1: Schematic of our sample structures and experimental technique. The samples are composed of metal grating on top of substrates of interests and are measured by an ultrafast optical time-domain thermoreflectance technique in the RK lab at MIT.

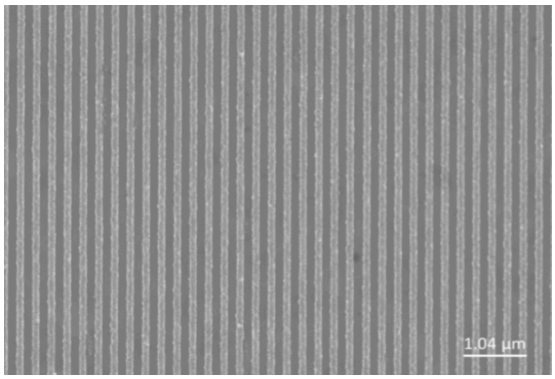

▲ Figure 2: Fabricated ~100 nm wide (period = 260nm) one-dimensional aluminum metal grating on top of a $Nb_{0.95}Ti_{0.05}FeSb$ substrate using the ebeam machine Elionix in Microsystems Technology Laboratories at MIT.

FURTHER READING

- L. Zeng and G. Chen, "Disparate Quasiballistic Heat Conduction Regimes from Periodic Heat Sources on a Substrate," *Journal of Applied Physics*, vol. 116, pp. 064307, 2014.
- Y. Hu, L. Zeng, A. J. Minnich, M. S. Dresselhaus, and G. Chen, "Spectral Mapping of Thermal Conductivity through Nanoscale Ballistic Transport," *Nature Nanotechnology*, vol. 10, pp. 701, 2015.
- L. Zeng, K. C. Collins, Y. Hu, M. N. Luckyanova, A. A. Maznev, S. Huberman, V. Chiloyan, J. Zhou, X. Huang, K. A. Nelson, and G. Chen, "Measuring Phonon Mean Free Path Distributions by Probing Quasiballistic Phonon Transport in Grating Nanostructures," *Scientific Reports*, vol. 5, pp. 17131, 2015.

Quantitative Analysis and Modeling of Templated Solid-State Dewetting of Thin Single-Crystal Ni Films

Y. A. Shin, K. Keane, G. H. Kim, W. C. Carter, C. V. Thompson
Sponsorship: NSF

It has been shown that templated solid-state dewetting of single crystal films (120 nm thick) can be used to make periodic complex structures with dimensions smaller than the templating patterns, making it a potential self-assembly method (Figure 1). A quantitative understanding of dewetting mechanisms is critical for design of self-assembled structures made through dewetting. In the past, we have studied corner, pinch-off, and Rayleigh instabilities. We are currently studying the fingering instability using single-crystal Ni films that have been patterned with edges lying along different in-plane crystallographic orientations. These edges were also patterned with periodic perturbations having various wavelengths. We found that some edges with specific in-plane crystallographic alignments were resistant to development of fingering instabilities, even with templating, and became straight as they retracted during dewetting. In the case of edges with other crystallographic alignments, we have shown that templating with patterned edge perturbations can be used to control the period of the fingering instability that develops the edges retract during dewetting (Figure 2). We are developing a kinetic Monte Carlo model to better understand mechanisms of the fingering instability.

In parallel with studies of templated fingering instabilities, we aim to generate smaller-scale dewetting structures using templated solid-state dewetting. Finer dewetting structures require thinner films. However, natural hole formation becomes easier as the film thickness is decreased, and uncontrolled formation of natural holes limits our ability to decrease the length-scale of dewetting structures, as naturally forming holes interrupt processes controlled through templating. We are developing methods to identify the cause of natural hole formation and to control it. After achieving control of natural hole formation, we will study dewetting phenomenologies in ultra-thin single crystal films and test the potential of templated solid-state dewetting as a self-assembly method for fabrication of nanostructures.

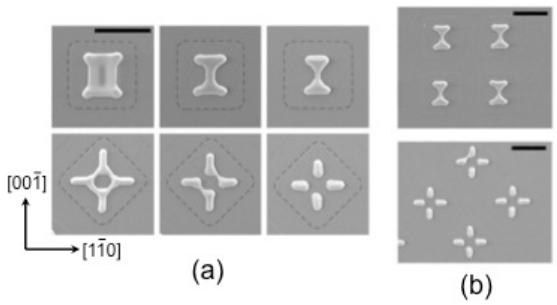

▲ Figure 1: (a) Partially dewetted patches patterned from a (100) Ni film into squares with different in-plane orientations; annealing time increases from left to right (b) Highly reproducible templated dewetting patterns. Scale bar: 10 μm.

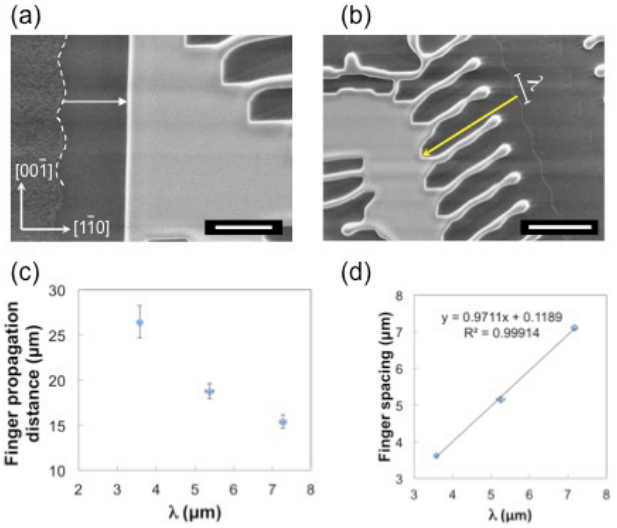

▲ Figure 2: (a) Edge retraction at patterned edge aligned along a kinetically stable orientation in Ni (110) film. (b) Development of fingering instability in a kinetically non-stable orientation. (c) Relationship between finger spacing as a function of intended perturbation, λ. Scale bar: (a) 5 μm and (b) 10 μm. λ: 5.364 μm.

FURTHER READING

- C. V. Thompson, "Solid-state Dewetting of Thin Films," *Annual Review of Materials Research*, vol. 42, pp. 399-434, 2012.
- R. V. Zucker, G. H. Kim, J. Ye, W. C. Carter, and C. V. Thompson, "The Mechanism of Corner Instabilities in Single-crystal Thin Films During Dewetting," *Journal of Appl. Phys.*, vol. 119, pp. 125306, 2016.
- G. H. Kim and C. V. Thompson, "Effect of Surface Energy Anisotropy on Rayleigh-like Solid-state Dewetting and Nanowire Stability," *Acta Materialia*, vol. 84, pp. 190, 2015.

Optimization of Vertically-Aligned CNT Carpets' Macro- and Nano-properties for Supercapacitor and Capacitive Deionization

M. Hashempour, H. Mutha, E. N. Wang, C. V. Thompson
Sponsorship: MITEI, Progetto Roberto Rocca

The science and technology of water desalination is receiving increasingly intensive attention due to human population growth and subsequent growing demands in domestic, industrial and agricultural sectors. Currently, desalination technology relies mainly on energy intensive techniques such as multi-stage flash (MSF), multi-effect distillation (MED), and reverse osmosis (RO). Capacitive deionization (CDI) is an emerging high-efficiency charge-based desalination technique with the ability to remove a wide range of ionic contaminants with high recovery rates. In CDI, an electrical potential difference is maintained between high-surface-area electrodes as a salt water stream passes through them, resulting in adsorption of anions and cations at the surface of positively and negatively polarized electrodes, respectively. Since CDI removes salt ions from water rather than treating the bulk water molecules, it requires much less energy than competing techniques. One of the main research directions in the field of CDI is development of electrode materials with high electrical conductivity, electrochemical stability, and morphologies allowing for a maximized surface area along with a minimized distance for ionic migration. In this project, we investigated the optimization of vertically aligned carbon nanotube (CNT) carpets for this application. CNTs were synthesized via chemical vapor deposition (CVD) and over a wide range of growth variables. We realized that the flow rate or partial pressure of the carbon precursor gas (C_2H_4 in our work) has the most fundamental effect on a carpet's macro-properties such as areal and volumetric density due to the modification of the number of CNT walls as well as their number density (Figure 1 a-d). Electrochemical studies of these CNTs in a supercapacitor set-up (Figure 2 a-b) confirm the highest gravimetric capacities (up to 25% compared to other CNTs) are found for CNTs grown at the lowest C_2H_4 flow rates, which provided the highest specific surface area and lowest number of CNT walls. The highest volumetric capacitance (by a factor of 2 compared to other CNTs) was, in contrast, found for CNTs grown at higher C_2H_4 flow rates, which provided the highest number density and lowest inter-CNT spacing. Preliminary CDI experiments were carried out, and successful capacitive desalination via these electrodes was demonstrated (Figure 2 c). More detailed parametric studies of the CDI performance along with development of an ion transport model are underway.

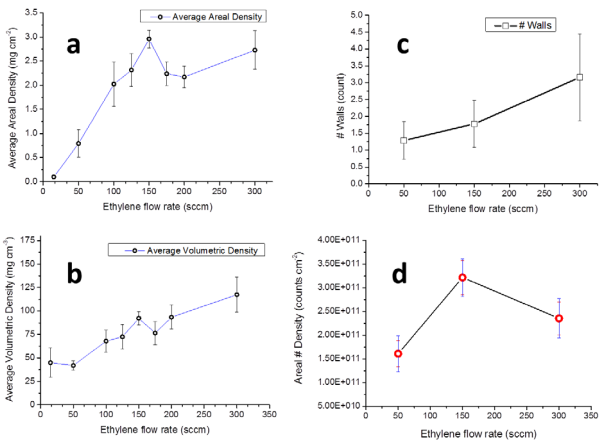

▲Figure 1: (a) areal density and (b) volumetric density of CNT carpets, (c) average number of walls and (d) number density of CNTs.

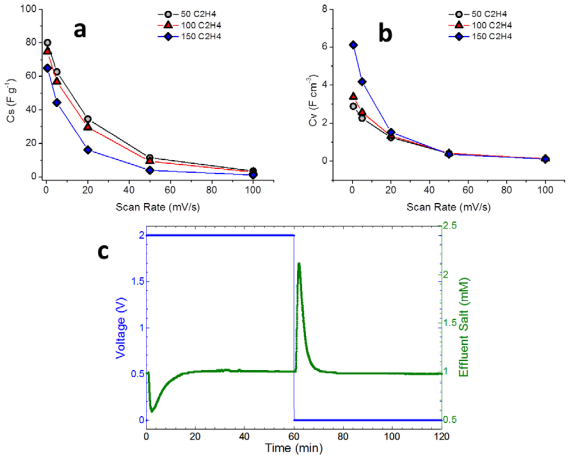

▲Figure 2: (a) gravimetric and (b) volumetric capacitance of CNTs in 50 mM NaCl solution, and (c) demonstration of salt concentration decrease in the brine flow upon the application of potential (adsorption) and its increase upon removal of the potential (desorption).

FURTHER READING

- M. A. Shannon, P. W. Bohn, M. Elimelech, J. G. Georgiadis, B. J. Mariñas, and A. M. Mayes, "Science and Technology for Water Purification in the Coming Decades," *Nature*, vol. 452, pp. 301–310, 2008.
- M. E. Suss, S. Porada, X. Sun, P. M. Biesheuvel, J. Yoon, and V. Presser, "Water Desalination via Capacitive Deionization: What Is It and What Can We Expect from It?" *Energy Env. Sci.* vol. 8, pp. 2296–2319, 2015.

Liquid Spreading in Ceramic-Coated Carbon Nanotube Films and Patterned Microstructures

H. Zhao, A. J. Hart
Sponsorship: NIH

We study the capillary-driven liquid spreading behavior on films and patterned microstructures of ceramic-coated vertically aligned carbon nanotubes (CNTs) (see Figure 1). The nanoscale porosity and micro-scale dimensions of the CNT structures, which can be precisely varied by the fabrication process, enable quantitative measurements that can be related to analytical models of the spreading behavior. Moreover, the alumina coating deposited conformally on the CNTs by atomic layer deposition (ALD) prevents capillary-induced deformation of the CNTs upon wetting and recession of the meniscus, which has complicated previous studies of this topic. CNT samples are fabricated on quartz substrates, enabling optical imaging of the contact line from the bottom of the substrate. A power-law liquid spreading behavior is observed on non-patterned CNT substrates and is explained using a scaling model based on the balance of capillary driving force and the viscous drag force (see Figure 2). Using these insights, we design micropatterned surfaces with controllable spreading rates and study the pinning-depinning behavior of the contact line. The nanoscale porosity, controllable surface chemistry, and mechanical stability of coated CNTs provide significantly enhanced liquid-solid interfacial area compared to solid microstructures. As a result, these surface designs may be useful for applications such as phase-change heat transfer, biomolecule capture, and electrochemical energy storage.

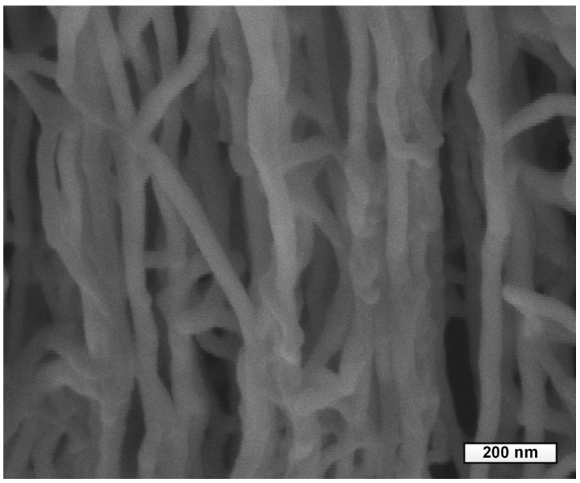

▲ Figure 1: Scanning electron microscope image showing side view of a vertically aligned CNT forest conformally coated with 15-nm-thick Al_2O_3 by ALD.

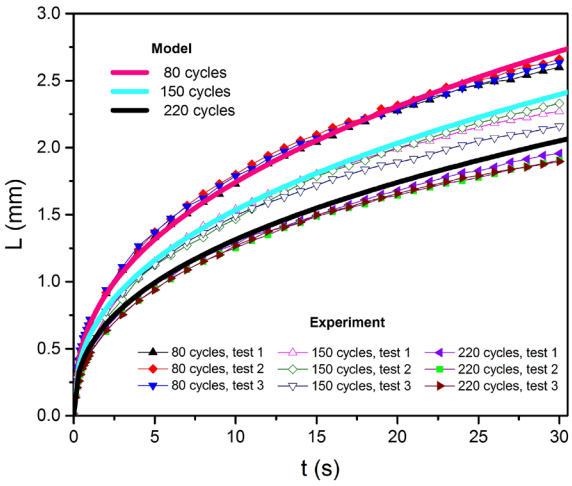

▲ Figure 2: Modeling and experimental measurement of liquid spreading on CNT forest with different Al_2O_3 coating thicknesses, showing a power-law scaling behavior.

FURTHER READING

- A. Brieland-Shoultz, S. Tawfick, S. J. Park, M. Bedewy, M. R. Maschmann, J. W. Baur, and A. J. Hart, "Scaling the Stiffness, Strength, and Toughness of Ceramic-Coated Nanotube Foams into the Structural Regime," *Advanced Functional Materials*, vol. 24, pp. 5728–5735, 2014.

Influence of Density Gradients on the Thermal Conductivity and Mechanical Compliance of Carbon Nanotube Forests

C. JacoS. Schiffres, S. Huberman, J. Li, G. Chen, A. J. Hart

Vertically aligned carbon nanotubes (VACNTs), often called CNT "forests," show promise to enable high performance thermal interface materials based on the thermal properties of individual CNTs and their collective mechanical compliance. Measurements of the thermal conductivity of individual, suspended CNTs have given values as high as 3000 $Wm^{-1}K^{-1}$; however, the thermal conductivities of CNT forests have varied widely, from 0.5 to 267 $Wm^{-1}K^{-1}$. Previous studies have shown the influence of boundary resistances, phonon scattering at CNT-CNT contacts, and intrinsic CNT defects on individual and collective CNT thermal properties. However, understanding of the collective growth of CNT forests, particularly of height-dependent morphology and density variations, has not been related to direct measurements of thermal conductivity. Such knowledge is important to improve the CNT growth process to give improved forest thermal conductivity and to engineer the mechanical and thermal properties of CNT-based thermal interfaces for specific applications.

Using frequency-domain thermoreflectance (FDTR), we characterize the thermal conductivity of CVD-grown VACNTs. FDTR is a non-contact method that uses continuous wave (CW) lasers to induce local heating in a thin film while measuring temperature response due to temperature-dependent reflectance changes in the sample. Owing to the height of the VACNT forests grown, from 10's µm to 100's µm, we treat them as thin films for the purpose of FDTR measurements. From our group's previous studies on the stages of CNT forest growth, we understand that density gradients occur along the height of the forest. As such we model these gradients as discrete layers within the forest for the purpose of thermal analysis. The resulting data were compared to known height and density gradients with the VACNTs to show correlation between macroscopic forest properties and the impact on thermal performance. Additionally, we perform compressive modulus testing to correlate thermal and mechanical performance of the forests.

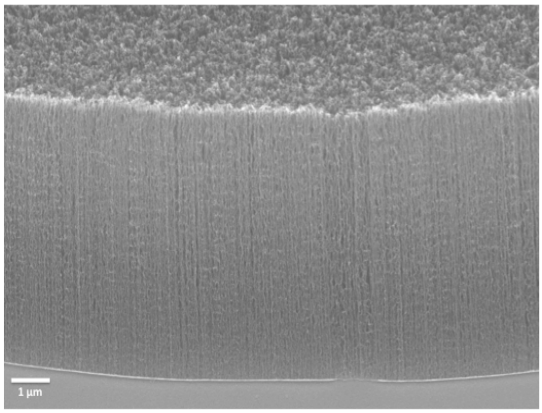

▲ Figure 1. Typical view of CNT forest edge. Known density variations occur along height of the forest.

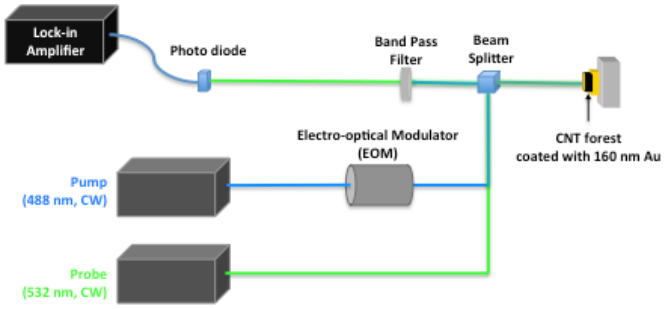

▲ Figure 2. Schematic of FDTR setup for thermal characterization of CNT forest. 160 nm of Au sputtered on top of forest acts as thermal transducer. The reflectance of this layer changes with temperature, which is recorded by the photodiode.

FURTHER READING

- M. Bedewy, E. R. Meshot, M. J. Reinker, and A. J. Hart, "Population Growth Dynamics of Carbon Nanotubes," *ACS Nano,* vol. 5, no. 11, pp. 8974–89, 2011.
- P. Kim, L. Shi, A. Majumdar, and P. McEuen, "Thermal Transport Measurements of Individual Multiwalled Nanotubes," *Physical Review Letters,* vol. 87, no. 21, p. 215502, 2001.
- Y. Gao, A. M. Marconnet, R. Xiang, S. Maruyama, and K. E. Goodson, "Heat Capacity, Thermal Conductivity, and Interface Resistance Extraction for Single-walled Carbon Nanotube Films using Frequency-domain Thermoreflectance," *IEEE Transactions on Components, Packaging and Manufacturing Technology,* vol. 3, no. 9, pp. 1524–1532, 2013.

Predictive Synthesis of Freeform Carbon Nanotube Microarchitectures by Strain-Engineered Chemical Vapor Deposition

S. J. Park, H. Zhao, S. Kim, M. De Volder, A. J. Hart
Sponsorship: AFOSR, NSF, NIH

High throughput fabrication of microstructured surfaces with multi-directional, re-entrant, or otherwise curved features is becoming increasingly important for applications such as phase change heat transfer, adhesive gripping, and control of electromagnetic waves. Toward this goal, curved microstructures of aligned carbon nanotubes (CNTs) can be fabricated by engineered variation of the CNT growth rate within each microstructure, such as by patterning of the CNT growth catalyst partially upon a layer that retards the CNT growth rate. Here, we develop a finite-element simulation framework for predictive synthesis of complex CNT microarchitectures by this strain-engineered growth process. The simulation is informed by parametric measurements of the CNT growth kinetics and the anisotropic mechanical properties of the CNTs, and it predicts the shape of CNT microstructures with impressive fidelity. Moreover, the simulation allows us to visualize the internal stress distribution that results from extreme deformation of the CNT structures during growth and shows that delamination of the interface between the differentially growing segments occurs at a critical shear stress. Guided by these insights, we perform experiments to study the time- and geometry-dependent stress development and show that corrugating the interface between the segments of each microstructure mitigates the interface failure. Last, we present a methodology for 3D microstructure design based on "pixels" that prescribe directionality to the resulting microstructure and show that this framework enables the predictive synthesis of more complex architectures including twisted and truss-like forms.

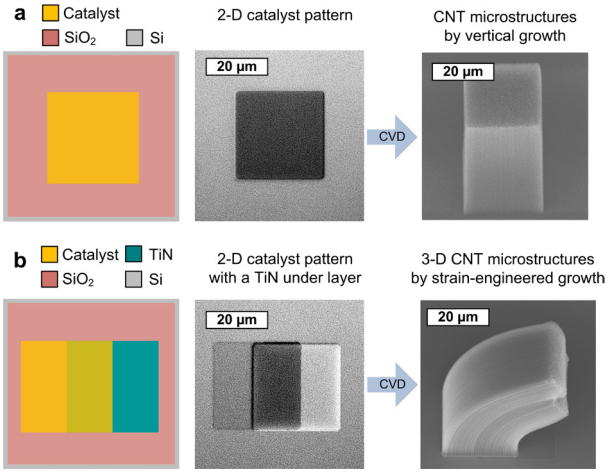

▲Figure 1: Catalyst pattern design and exemplary results for (a) vertical and (b) curved (strain-engineered) CNT microstructure growth.

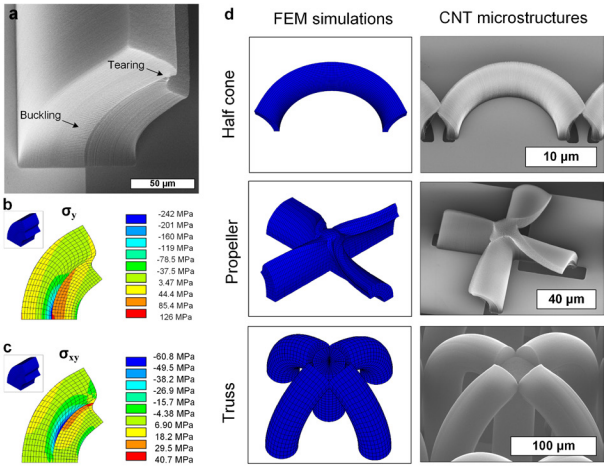

▲Figure 2: (a) SEM image of curved CNT microstructure showing tearing at the top of the interface and local CNT buckling lower along the interface. (b)-(c) Finite element method (FEM) simulations of axial and shear stress distributions. (d) Comparison of FEM simulations to SEM images for the "half cone," "propeller," and "microtruss" CNT microstructures.

FURTHER READING

- M. De Volder, S. J. Park, S. Tawfick, and A. J. Hart, "Strain-Engineered Manufacturing of Freeform Carbon Nanotube Microstructures," *Nature Communications*, vol. 5, pp. 4512, 2014.
- J. Meaud, T. Sain, B. Yeom, S. J. Park, A. Brieland-Shoultz, G. Hulbert, N. A. Kotov, A. J. Hart, E.M. Arruda, and A.M. Waas, "Simultaneously High Stiffness and Damping in Nanoengineered Microtruss Composites," *ACS Nano*, vol. 8, pp. 3468-3475, 2014.

Verified Nanoscale Engineering of Diamond Nitrogen-Vacancy Centers

M. E. Trusheim, D. Scarabelli, O. Gaathon, S. J. Wind, D. Englund
Sponsorship: AFOSR, DTRA

The nitrogen-vacancy (NV) center in diamond has been intensely investigated as a spin qubit in quantum information processing applications. Central to the implementation of these schemes is engineering NV centers on the scale of coherent dipole-dipole coupling. Here, we present and characterize a fabrication technique for creating arrays of NV centers on the 10-nm scale through implantation masking.

We begin with an Au/Cr stack on ultra-pure diamond and pattern apertures in a spin-coated PMMA layer using electron beam lithography (Figure 1a). After development, we perform angular evaporation of Ti, which serves as a hard mask for pattern transfer into the Au layer though Ar milling. The resulting nano-apertures have a diameter of ~10 nm and a 40- nm pitch (Figure 1b). We then implant ^{15}N with a predicted depth of 10 nm and masking isolation of $5*10^4$. Finally, we remove the masking layers and form NVs through wet chemical processes and thermal annealing.

Following fabrication, we image the resulting NV centers below the optical diffraction limit through wide-field super resolution microscopy. This technique, illustrated in Figure 1c-e, isolates photoluminescence (PL) from individual NV centers through selective magnetic resonance addressing (Figure 1d), allowing the reconstruction of their positions (Figure 1e). We then collect statistics on NV positions for different implantation aperture configurations, verifying that the produced NVs match the predicted distribution (Figure 1f).

We characterize the spin coherence properties of the NVs created through our process with Hahn echo and CPMG-N sequences. The array-average coherence time $T_{2,echo}$ = 10 μs was increased to $T_{2,CPMG-128}$ = 67 μs, with a relation $T_{2,CPMG-N} = T_{2\_1} * N^{\lambda}$ and scaling parameter λ= 0.69±0.05 describing the NV performance (Figure 1h). The NV coherence times achieved allow entanglement of NV pairs over a distance of 10 nm, comparable to the measured positioning accuracy.

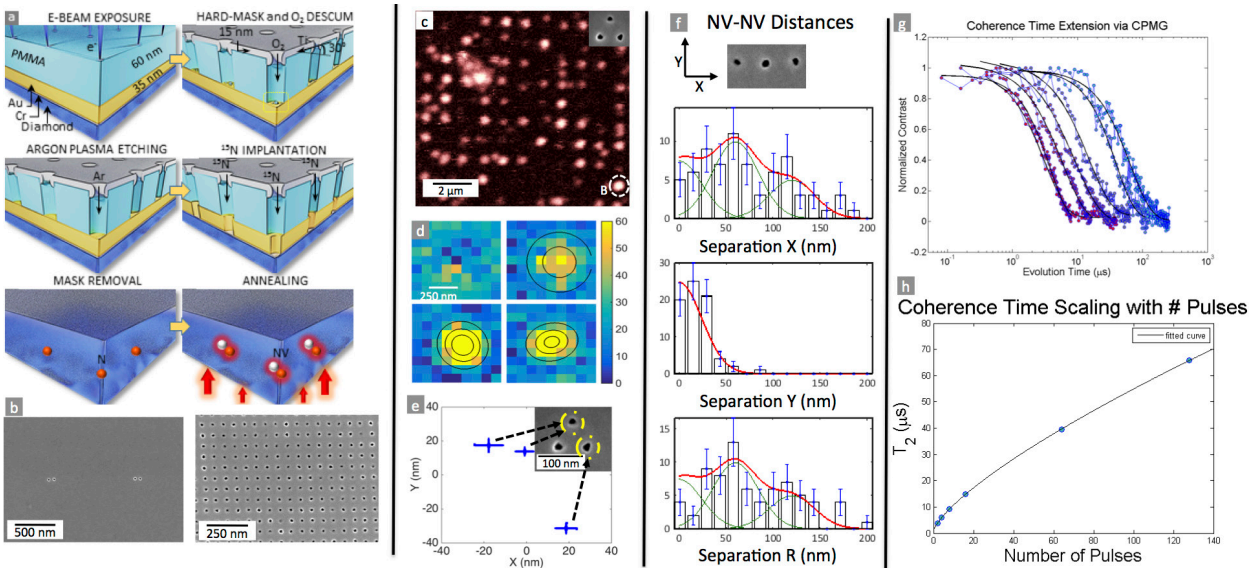

▲ Figure 1: Engineered NV arrays. a) Fabrication process. b) Resulting mask apertures. c) PL image of an array of triangular aperture configurations. d) Spin contrast images of the indicated site in c). e) Reconstructed NV positions. f) Statistics on pairwise NV-NV spacings for implantation through a linear triple aperture configuration h) Scaling of T_2 with number of pulses.

FURTHER READING

- I. Bayn, *et al*, "Generation of Ensembles of Individually Resolvable Nitrogen Vacancies Using Nanometer-scale Apertures in Ultrahigh-aspect Ratio Planar Implantation Masks," *Nano Letters*, vol. 15, pp. 1751-1758, 2015.
- E. H. Chen, O. Gaathon, M. E. Trusheim, and D. R. Englund, "Wide-field Multispectral Super-resolution Imaging Using Spin-dependent Fluorescence in Nanodiamonds," *Nano Letters*, vol. 13, pp. 2073-2077, 2013.

Research on CMOS-Compatible High-K Dielectrics for Magnetic Memory

S. Kim, H. L. Tuller in collaboration with A. J. Tan, G. S. Beach
Sponsorship: CMSE/IRG, NSF

High-k dielectrics play a key role in modern microelectronic circuitry, given their ability to provide reduced leakage currents while providing adequate capacitance in ever smaller nano-dimensioned metal-oxide semiconductor field-effect transistor (MOSFET) devices. Recently, the Beach group at MIT demonstrated the ability to modulate the magnetic properties of transition metal thin films by electrical bias across thin films of Gd_2O_3. The reversible switching was demonstrated to be assisted by the electro-migration of oxygen ions to and away from the transition metal/Gd_2O_3 interface. This novel process, now called "magneto-ionic control" creates new opportunities for nonvolatile information storage. In this study, we have begun a more detailed examination of the properties of Gd_2O_3 and related oxides, to establish how their defects and nanostructures impact oxygen ion transport and, in turn, magneto-ionic device properties.

FURTHER READING

- U. Bauer, L. Yao, A. J. Tan, P. Agrawal, S. Emori, H.L. Tuller, S. van Dijken, and G. Beach, "Magneto-ionic Control of Interfacial Magnetism," *Nature Materials*, 14, 174-181, 2015.

Folding of Graphene Hinge Structures Dispersed in Solution

M. Hempel, T. Palacios, J. Kong
Sponsorship: AFOSR

Two-dimensional materials such as graphene, hexagonal boron nitride, and molybdenum disulfide have opened up a new chapter in electronics. They can be used to fabricate a variety of electronic devices from CMOS logic to photodetectors or sensors. Currently, however, devices made from 2D materials have been used only on flat surfaces, which do not exploit their full potential. Given the extreme thinness and flexibility of these materials, more sophisticated three-dimensional device structures can be imagined by using techniques such as folding and cutting, analogous to origami techniques.

In order to realize this vision, we are investigating the folding of strips of graphene in a controlled manner. The fabrication process of these hinges, as shown in Figure 1a-d, starts with an oxidized silicon piece with a sacrificial 40-nm- thick aluminum layer that is patterned by photolithography. Next, a monolayer of graphene is transferred and patterned into strips by a short oxygen plasma etching. Subsequently, a 50-nm-thick gold layer is deposited by electron beam evaporation and patterned by a lift-off process. The gold is used to anchor the graphene to the substrate on one side of the hinge as well as to stiffen the graphene film in between the joints. In the final step, the device is etched in a diluted (10%) hydrochloric acid solution, which dissolves the sacrificial aluminum layer and decouples the graphene from the surface.

After the fabrication process is completed, the silicon piece with graphene hinges is submerged in deionized water mixed with cholate hydroxide, which acts as a surfactant that keeps the graphene from sticking to itself.

So far, we have been able to pattern the graphene into strips and release them partially in solution. Figure 1e shows patterned and partially suspended graphene strips that were released from the substrate. The wrinkles and folds confirm that the strips are detached from the surface. In the future, our goal is to control this folding and buckling and to investigate the targeted folding of more advanced structures such as transistors, which would allow us to reduce the device footprint at equal performance.

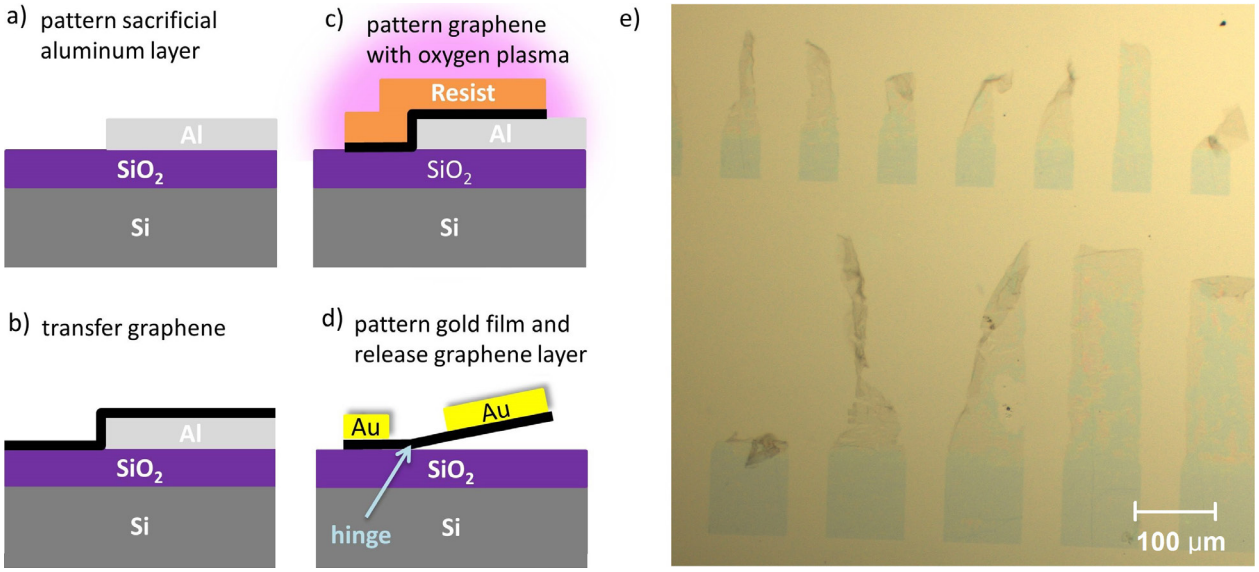

▲ Figure 1: a-d) Steps of fabricating a graphene hinge on an oxidized silicon substrate with gold film reinforcement, e) optical micrograph of partially floating graphene strips in solution. The wrinkles and folds confirm that the strips are detached from the surface.

FURTHER READING

- M. K. Blees, A. W. Barnard, P. A. Rose, S. P. Roberts, K. L. McGill, P. Y. Huang, A. R. Ruyack, J. W. Kevek, B. Kobrin, D. A Muller, and P. L. McEuen, "Graphene Kirigami," *Nature*, vol. 524, no. 7564, pp. 204-207, August 2015.
- J. Choi, H. J. Kim, M. C. Wang, J. Leem, W. P. King, and S. Nam, "Three-Dimensional Integration of Graphene via Swelling, Shrinking, and Adaptation," *Nano Letters*, vol. 15, pp. 4525–4531, June 2015.

Electrospray-Printed Graphene Oxide Nanostructured Humidity Sensor

A. P. Taylor, L. F. Velásquez-García
Sponsorship: Edwards Vacuum

Conductometric gas sensors based on the chemoresistive response of semiconducting metal oxide films are widely used due to their simplicity, flexibility in production, and broad applicability to many fields. Typically, the adsorption of a gas molecule on the surface of a metal oxide alters surface electronic properties, causing a change in electrical conductivity. Although many metal oxides could be used for gas sensing, only a few show the appropriate combination of adsorption ability, catalytic activity, sensitivity, and thermodynamic stability. These select metal oxides (e.g., SnO_2, TiO_2, and ZnO), however, are the least active from the catalytic point of view. To alleviate this problem, doping with redox-active noble metal nanoparticles, such as Pt, Au, and Pd, is done to enhance conductivity response. Unfortunately, noble metals are expensive, thereby precluding their use in low-cost applications. An appealing alternative material for reactive gas sensing is graphene oxide (GO) because of its high sensitivity to adsorbed surface species and compatibility with harsh environments.

We developed low-cost conductometric gas sensors t hat use an ultrathin film made of a matrix of GO nanoflakes as a transducing element. The devices were fabricated by lift-off metallization and near-room temperature, atmospheric pressure electrospray printing using a shadow mask. The sensors detect humidity at room temperature without requiring any post-heat treatment, harsh chemical reduction, or doping with metal nanoparticles. The printed GO devices (Figure 1) show a linear relationship between the resistance of the GO sensors and relative humidity in the 10-60% range (Figure 2); considering that they were fabricated with different electrospray printing recipes, the similarity between the linear response of the two devices suggests a common underlying physical sensing mechanism dependent on the intrinsic properties of the material. The power consumption of the printed sensors was estimated at 6 µW or less in the 10-60% relative humidity range.

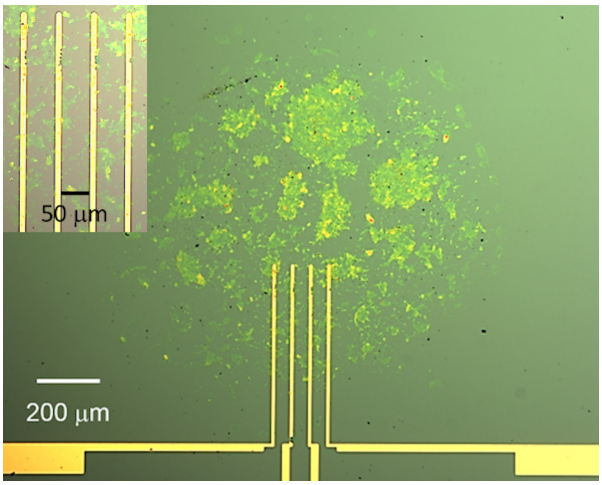

▲ Figure 1: Optical micrograph of a conductometric GO humidity sensor with a four-point probe electrode configuration and an inset showing a close-up view of the active area (top left corner). From A. P. Taylor and L. F. Velásquez-García, *Nanotechnology*, 2015.

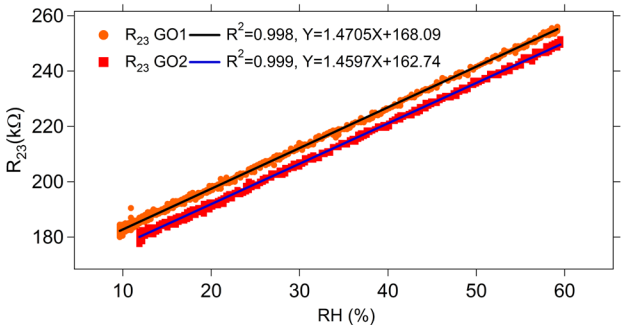

▲ Figure 2: Resistance versus relative humidity for two electrospray-printed GO sensors. From A. P. Taylor and L. F. Velásquez-García, *Nanotechnology*, 2015.

FURTHER READING

- F. A. Hill, E. V. Heubel, P. Ponce de Leon, and L. F. Velásquez-García, "High-Throughput Ionic Liquid Ion Sources Using Arrays of Microfabricated Electrospray Emitters with Integrated Extractor Grid and Carbon Nanotube Flow Control Structures," *Journal of Microelectromechanical Systems*, vol. 23, no. 5, pp. 1237-1248, 2014.
- A. P. Taylor and L. F. Velásquez-García, "Electrospray-Printed Graphene Oxide Nanostructured Gas Sensors," *Nanotechnology*, vol. 26, pp. 505301-505309, 2015.
- A. P. Taylor and L. F. Velásquez-García, "Microwatt-Powered, Low-Cost, Printed Graphene Oxide Humidity Sensors for Distributed Network Applications," *PowerMEMS 2015, Journal of Physics: Conference Series*, vol. 660, pp. 12134-12139, 2015.

3D Printing of Electronic 2D Materials

E. McVay, T. Palacios
Sponsorship: NASA

In this project we are meshing 3D printing and inkjet technology to apply two-dimensional materials on a large scale to create "smart objects" that can sense and process their environment. We are modifying a 3D printer to give it inkjet and extrusion printing capabilities, as well as developing 2D material inks and designing the device and circuit applications that this system will be applied to make. The printer can extrude standard polylactic acid plastic, conductive filaments, and flexible substrate materials; it is also fitted with a STMicroelectronics inkjet head that is well suited for printing the 2D material inks (see Figure 1). Thus far we have focused on printing graphene oxide, molybdenum disulfide (MoS_2), and tungsten diselenide (WSe_2) flakes. The graphene oxide prints can be reduced to graphene via laser sintering to achieve a sheet resistance of 680 ohms/square; these traces can also function as strain sensors. We are developing MoS_2 dispersions with the goal of using this material to print the channel layer of a transistor, as MoS_2 transistors have shown even higher sensitivity than graphene in light and gas-sensing applications. Furthermore, we have developed WSe_2 dispersions which, when printed and contacted with platinum, show a photo-responsive current (see Figure 2). With WSe_2 and printed metals, we can begin to fabricate solar cells that can provide energy to the proposed sensing system. The end goal of this project is to demonstrate the use of 2D materials in sensor, energy harvesting, and energy storage circuit blocks to create "smart skins" that can be used in applications from monitoring the structural integrity of machinery to keeping track of a person's health through smart textiles.

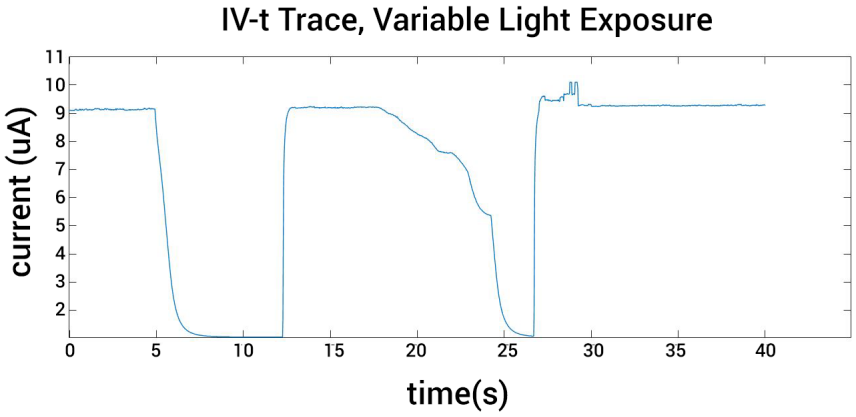

◀ Figure 1: Graphene-WSe2-platinum light sensor (area = 0.25 cm^{-2}) current output with response to pulsed light (200 W/cm^2), over time. Figure 1: The 3D printer with dual extruders and inkjet printhead (attached behind the dual extruders, shown in the upper right-hand corner).

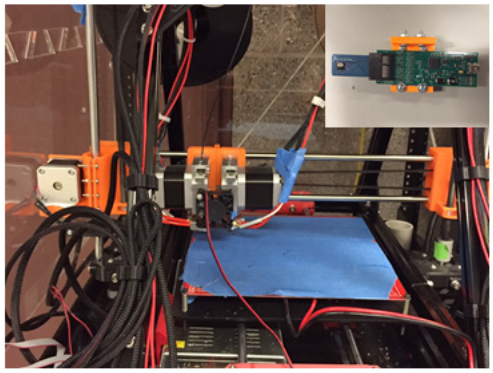

◀ Figure 2: The 3D printer with dual extruders and inkjet printhead (attached behind the dual extruders, shown in the upper right-hand corner).

FURTHER READING

- M. F. El-Kady, V. Strong, S. Dubin, and R. B. Kaner, "Laser Scribing of High-Performance and Flexible Graphene-Based Electrochemical Capacitors," *Science*, vol. 335, no. 6074, pp. 1326-1330, 2012.
- S. Wang, P. K. Ang, Z. Wang, A. L. L. Tang, J. T. L. Thong, and K. P. Loh, "High Mobility, Printable, and Solution-Processed Graphene Electronics," *Nano Letters*, vol. 10, pp. 92-98, 2010.
- D. Sarkar, W. Liu, X. Xie, A. Anselmo, S. Mitragotri, and K. Banerjee, "MoS2 Field-Effect Transistor for Next-Generation Label-Free Biosensors," *ACSNano*, vol. 8, no. 4, pp. 3992-4003, 2014.

A Rational Strategy for Transferring Graphene onto Rough Substrates

J.-Y. Hong, J. Kong
Sponsorship: NSF Center for Integrated Quantum Materials

Degradation in the intrinsic properties of chemical vapor deposition (CVD)-grown graphene, as a result of the imperfect transfer process, is a crucial issue that must be solved for successful applications of graphene. Here, we develop a very simple, yet effective, approach, based on distinctive features (i.e., physical, mechanical, and chemical properties) of ethylene vinyl acetate (EVA) as a support/carrier material, for transferring CVD-grown graphene from a growth substrate onto rough substrates. This novel and facile method not only results in satisfactory transfer on substrates with terraces or grooves, but also gives rise to a successful result for uneven growth substrates (textured and also crumpled).

Under our experimental condition, the elastic modulus (E) values of the polymer/graphene films were estimated as 995.0 ± 5.0 and 46.5 ± 1.5 MPa for the poly(methyl methacrylate) (PMMA)/graphene and EVA/graphene films, respectively (Figures 1a and b). It should be noted that the approximately one-twentieth-lower E value of the EVA/graphene film implies a tremendously lower stiffness in comparison with the PMMA/graphene film, and it is also anticipated that the EVA/graphene film would follow the surface of the underlying substrate much better and have a tighter attachment to the surface (Figure 1c and d).

Figure 2 shows the optical microscopy (OM) and atomic force microscopy (AFM) images of graphene on SiO_2/Si substrates obtained by the conventional PMMA-supported transfer process and the EVA transfer process. White arrows in Figure 2a and c indicate the PMMA residues on graphene as are typically observed while for the EVA case such residues can hardly be found. Furthermore, wrinkles can be clearly seen in the PMMA-transferred graphene (black arrow in Figure 2a and c) but are much less frequently seen in the hot-water bath EVA-transferred graphene. Consequently, the graphene transferred with EVA support/carrier material exhibits superior electrical performance compared with most presently used transfer methods.

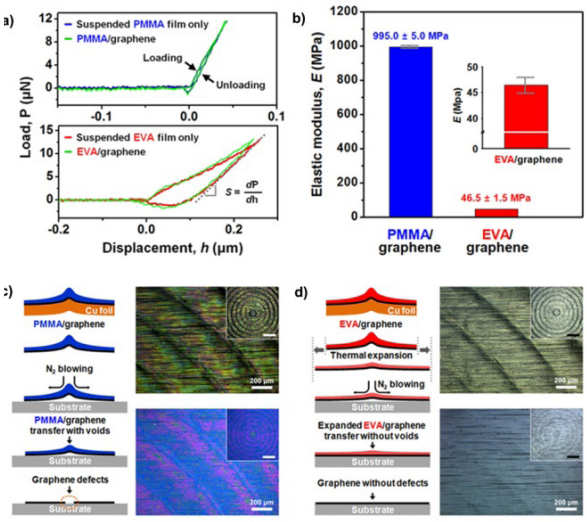

▲ Figure 1: Representative (a) load–displacement curves and (b) E values for polymer/graphene films. Comparison of thermal expansion effects between (c) PMMA/graphene and (d) EVA/ graphene during the transfer process.

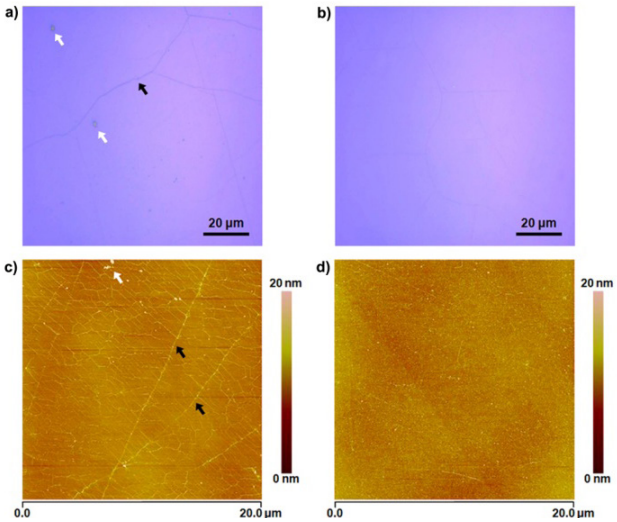

▲ Figure 2: The OM and AFM images of monolayer graphene transferred to 300-nm SiO_2/Si substrate by using the (a, c) PMMA-supported and (d) EVA-supported transfer methods.

FURTHER READING

- J.-Y. Hong, Y. C. Shin, A. Zubair, Y. Mao, T. Palacios, M. S. Dresselhaus, S. H. Kim, and J. Kong, "A Rational Strategy for Graphene Transfer on Substrates with Rough Features," *Advanced Materials*, vol. 28, pp. 2382-2392, 2016.

Large-Area Synthesis of High-Quality Uniform Few-Layer $MoTe_2$

L. Zhou, K. Xu, A. Zubair, J. Kong, M. S. Dresselhaus
Sponsorship: NSF, ONR

Two-dimensional transition metal dichalcogenides (TMDs) have been attracting increasing interest owing to their unique structures and remarkable properties, which make them promising materials for a wide range of applications related, for example, to electronics, optoelectronics, valleytronics, spintronics, and catalysis. Because of the smaller bandgap compared with other group VI TMDs, single- and few-layer $MoTe_2$ holds promise for use in easily controllable ambipolar field-effect transistors and extends the operating range of TMD optoelectronic devices from the visible to the near-infrared range. In particular, the bandgap, which is quite close to that of Si (~ 1.1 eV); the strong absorption throughout the solar spectrum; and the strong spin-orbit coupling suggest that $MoTe_2$ is a highly attractive material for use in electronic devices, photovoltaic devices, spintronic, and valley-optoelectronic devices. A crucial step toward the practical application of $MoTe_2$ in electronics and optoelectronics is the controlled production of high-quality, large-area, and atomically thin $MoTe_2$ films. Thus far, single- and few-layer $MoTe_2$ have been achieved only using "top-down" exfoliation methods. Thus a technology for the mass-production of high-quality, large-area, and atomically thin $MoTe_2$ films is highly desirable. Our group has developed a chemical vapor deposition (CVD) synthesis to produce large-area, uniform, and highly crystalline few-layer 2H and 1T´ $MoTe_2$ films. We found that these two different phases of $MoTe_2$ can be grown based on the choice of Mo precursor. The resulting $MoTe_2$ phase and the efficiency of the tellurization are both strongly dependent on the oxidation state of the Mo precursor. Mo film was deposited onto a SiO_2/Si substrate by electron beam evaporation. Then, the Mo film was fully oxidized in air and changed to MoO_3. The resulting MoO_3 film was placed in a ceramic crucible containing Te powder in CVD system and was tellurized into a $MoTe_2$ film after annealing in tellurium vapor at 700 ˚C. The film is uniform and continuous across the whole area, as can be seen from the homogeneous color contrast in the image (Figure 1). When using Mo (instead of MoO_3) as a precursor, a 1T′ $MoTe_2$ film (Figure 2) can also be grown under the same growth conditions mentioned above. Due to the high crystalline structure, the as-grown few-layer 2H $MoTe_2$ films display electronic properties that are comparable with those of mechanically exfoliated MoTe2 flakes. Since our high-quality, atomically thin $MoTe_2$ films are highly homogenous, and the size of the films is limited only by the size of the substrate, our growth method paves the way for large-scale application of $MoTe_2$ in high-performance nanoelectronics and optoelectronics.

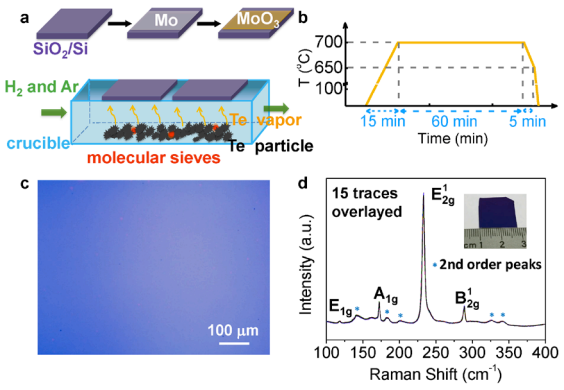

▲ Figure 1: Synthesis of 2H $MoTe_2$. (a) Illustration of $MoTe_2$ CVD process. (b)Temperature-controlled sequence used for a typical growth of $MoTe_2$. (c)Typical optical image of an as-synthesized $MoTe_2$ film on a 300nm SiO_2/Si substrate. (d)Raman spectra of a $MoTe_2$ film at 15 different locations on the sample. Inset: Photograph of a $MoTe_2$ film on a 1.6×1.8 cm^2 SiO_2/Si substrate.

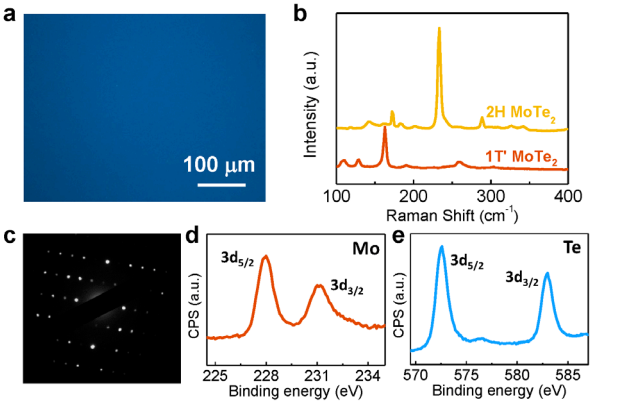

▲ Figure 2: Characterizations of the resulting 1T′ $MoTe_2$ film. (a) Typical optical image of an as-synthesized 1T′ $MoTe_2$ film on 300nm SiO_2/Si. (b) Raman spectra of 1T′ (red) compared to 2H (orange) $MoTe_2$ films. (c) SAED pattern for the 1T′ $MoTe_2$. (d & e) High-resolution XPS spectra for Mo 3d (d) and Te 3d (e) spectra of a 1T′ $MoTe_2$ film.

FURTHER READING

- Y.-F. Lin, Y. Xu, S.-T. Wang, S.-L. Li, M. Yamamoto, A. Aparecido-Ferreira, W. Li, H. Sun, S. Nakaharai, W.-B. Jian, K. Ueno, K. Tsukagoshi, "Ambipolar $MoTe_2$ Transistors and Their Applications in Logic Circuits," *Adv. Mater.*, vol. 26, issue 20, pp. 3263, 2014.
- C. Ruppert, O. B. Aslan, and T. F. Heinz, "Optical Properties and Band Gap of Single- and Few-Layer $MoTe_2$ Crystals," *Nano Letters*, vol. 14, no 11, pp. 6231, 2014.
- D. H. Keum, S. Cho, J. H. Kim, D.-H. Choe, H.-J. Sung, M. Kan, H. Kang, J.-Y. Hwang, S. W. Kim, H. Yang, K. J. Chang, Y. H. Lee, "Bandgap Opening in Few-Layered Monoclinic $MoTe_2$," *Nat. Phys.*, vol. 11, pp. 482, 2015.